Journal of Translational Medicine

RESEARCH

Open Access

Comprehensive analysis of scRNA-seq and bulk RNA-seq reveals the non-cardiomyocytes heterogeneity and novel cell populations in dilated cardiomyopathy

Siyu He[1,2,3], Chunyu Li[1,2,3], Mingxin Lu[1,2,3], Fang Lin[1,2,3], Sangyu Hu[1,2,3], Junfang Zhang[3], Luying Peng[1,2,3,4*] and Li Li[1,2,3,4*]

Abstract

Background Dilated cardiomyopathy (DCM) is one of the most common causes of heart failure. Infiltration and alterations in non-cardiomyocytes of the human heart involve crucially in the occurrence of DCM and associated immunotherapeutic approaches.

Methods We constructed a single-cell transcriptional atlas of DCM and normal patients. Then, the xCell algorithm, EPIC algorithm, MCP counter algorithm, and CIBERSORT method were applied to identify DCM-related cell types with a high degree of precision and specificity using RNA-seq datasets. We further analyzed the heterogeneity among cell types, performed trajectory analysis, examined transcription factor regulatory networks, investigated metabolic heterogeneity, and conducted intercellular communication analysis. Finally, we used bulk RNA-seq data to confirm the roles of M2-like2 subpopulations and GAS6 in DCM.

Results We integrated and analyzed Single-cell sequencing (scRNA-seq) data from 7 DCM samples and 3 normal heart tissue samples, totaling 70,958 single-cell data points. Based on gene-specific expression and prior marker genes, we identified 9 distinct subtypes, including fibroblasts, endothelial cells, myeloid cells, pericytes, T/NK cells, smooth muscle cells, neuronal cells, B cells, and cardiomyocytes. Using machine learning methods to quantify bulk RNA-seq data, we found significant differences in fibroblasts, T cells, and macrophages between DCM and normal samples. Further analysis revealed high heterogeneity in tissue preference, gene expression, functional enrichment, immunodynamics, transcriptional regulatory factors, metabolic changes, and communication patterns in fibroblasts and myeloid cells. Among fibroblast subpopulations, proliferative F3 cells were implicated in the fibroblast transition process in DCM, while myofibroblast F6 cells promoted the fibroblast transition to a late cell state in DCM. Additionally, two subpopulations of M2 macrophages, M2-like1 and M2-like2, were identified with distinct features. The M2-like2 cell subpopulation, which was enriched in glycolysis and fatty acid metabolism, involved in inflammation

*Correspondence:
Luying Peng
luyingpeng@tongji.edu.cn
Li Li
lilirz@tongji.edu.cn
Full list of author information is available at the end of the article

inhibition and fibrosis promotion. Cell–cell communication analysis indicated the GAS6-MERTK axis might exhibit interaction between M2 macrophage and M2-like1 macrophage. Furthermore, deconvolution analysis for bulk RNA-seq data revealed a significant increase in M2-like2 subpopulations in DCM, suggesting a more important role for this cell population in DCM.

Conclusions We revealed the heterogeneity of non-cardiomyocytes in DCM and identified subpopulations of myofibroblast and macrophages engaged in DCM, which suggested a potential significance of non-cardiomyocytes in treatment of DCM.

Keywords Dilated cardiomyopathy (DCM), Single-cell RNA sequencing (scRNA-seq), Bulk RNA sequencing (Bulk RNA-seq), Non-cardiomyocytes, Heterogeneity

Background

Dilated cardiomyopathy characterized by left ventricular dilation associated with systolic dysfunction is the most common cardiomyopathy worldwide. DCM also involves having diastolic dysfunction and right ventricular impairment, putting patients at risk of left ventricular failure, right ventricular failure, or both, either as primary or secondary conditions [1]. Immunohistological evidence has shown that inflammation is an independent predictor of survival in DCM patients in clinical and experimental investigations [2, 3]. Therefore, precise characterization and quantification of non-cardiomyocytes cell subtypes are necessary in personalized treatment of DCM.

The heart is composed of different cell populations, each with specific roles and regulations to maintain the organ function. Cardiomyocytes constitute the majority of heart tissue [4], but only have 25–35% of all heart cells [5]. On the other hand, Pinto A R et al. using immunohistochemistry revealed that endothelial cells account for more than 60% and fibroblasts are less than 20% of non-cardiomyocyte populations, making endothelial cells the most common cell type in the adult heart [6], this estimated number of endothelial cells contradicts studies that have previously characterized heart cellular composition, where findings suggested that fibroblasts constitute the principal non-cardiomyocytes populations [4, 5, 7, 8]. The proportions of these cell populations are still a matter of debate [4, 9, 10], such as the communication and roles of these cell populations in maintaining heart function remain largely unknown [11, 12]. Single-cell sequencing as an innovative tool in biomedical research [13] has been performed to conduct a comprehensive gene expression profile analysis for 10,519 non-cardiomyocytes in adult mouse hearts, providing a panoramic view of the single-cell transcriptome of these cells [14, 15], in which the diversity of non-cardiomyocytes and new subpopulations of rare cells, such as mural cells and glial cells, were identified, offering significant research resources for further exploration of cell structure and function in the mammalian heart by generating an extensive network of intercellular communication. For example, mapping the intercellular communication network within the heart could discover the alternations that promote the development of a fibrotic cell microenvironment and cellular communication following angiotensin II treatment. On the other hand, single-cell sequencing technology also holds the potential to reveal disease mechanisms by leveraging findings from whole-genome association studies or analyzing different cell types and unique characteristics of the heart in terms of cell composition, signaling interactions, and transcriptomic dynamics that contribute to cardiac regeneration [16]. The comparison of single-cell transcriptional differences between healthy and diseased adult hearts has identified cell type-specific changes that can help to underpin cellular processes related to cardiac biology and pathophysiology. Thus, the application of this technology may lead to the discovery of new therapeutic targets associated with heart disease [17]. A comprehensive understanding of the changes in the microenvironment of diseased hearts will be a fundamental step in determining future treatment methods. However, the limitations in the number of DCM samples, as well as the cells and tools available for data analysis, make the early knowledge obtained from previous studies about the landscape of non-cardiomyocytes in DCM still being insufficient.

Here, we integrated single-cell RNA sequencing data from 70,958 cells from 7 human DCM samples and 3 normal samples. Based on various advanced analysis tools, we identified a serious of features such as tissue preferences, gene expression, functional enrichment, immune dynamics, transcriptional regulators, metabolic changes, and communication patterns underlying non-cardiomyocytes heterogeneity, and further found that DCM was associated with the M2-like2 macrophage subpopulation, which may serve as a potential therapeutic target for precision medicine of DCM.

Methods

Data acquisition

The scRNA-seq datasets were obtained from Gene Expression Omnibus (GEO) database: GSE183852 (https://www.ncbi.nlm.nih.gov/geo/query/acc.cgi?acc=GSE183852) and GSE145154 (https://www.ncbi.nlm.nih.gov/geo/query/acc.cgi?acc=GSE145154). Bulk RNA-seq datasets were downloaded from GEO database: GSE145154 (https://www.ncbi.nlm.nih.gov/geo/query/acc.cgi?acc=GSE141910), GSE1145 (https://www.ncbi.nlm.nih.gov/geo/query/acc.cgi?acc=GSE1145), and GSE116250 (https://www.ncbi.nlm.nih.gov/geo/query/acc.cgi?acc=GSE116250) and HubnerLab database (http://shiny.mdc-berlin.de/cardiac-translatome/) (Additional file 7: Table S1).

Comprehensive analysis of single cell datasets

ScRNA-seq datasets of human DCM and normal samples were downloaded from the GEO database. The raw gene expression matrix was converted into Seurat objects using the Seurat R (version 4.2.2) package. To exclude low-quality cells, we filtered cells that expressed between 500 and 4000 genes, and used the genes expressed in at least 3 cells for further analysis. The maximum number of genes and the percentage of mitochondrial genes (pctMT) were set to 10%. After the above quality control steps, we identified "anchors" across different batch samples to construct reference information. First, the datasets were merged into a Seurat object list using the merge and SplitObject functions. We standardized the data using the "PrepSCTIntegration" function and identified the top 2000 highly variable genes (HVGs) using the "SelectIntegrationFeatures" method. Next, we detected anchors by the "FindIntegrationAnchors" function with default parameters and integrated the batch processing expression matrices of all cells into Seurat objects using the "IntegrateData" function based on the previously identified anchors. Afterward, HVGs and the top 20 principal components were used for dimension reduction. The graph-based and k-mean-based clustering approaches implemented in the "FindNeighbor" function of the Seurat package were used for data clustering, with a K parameter of 30 and the "FindClusters" function with the "resolution" parameter set to 0.5.

Clusters were labeled according to their key marker genes or annotated as known cell subsets based on the literature, and were visualized with t-distributed stochastic neighbor embedding (t-SNE) by running dimensionality reduction with "RunTSNE", setting "dims" to 1:30. e. Any cluster that had multiple markers for two different cell types was manually eliminated as a doublet. The "FindAllMarkers" function utilized the Wilcoxon method to identify significantly expressed genes in each cell subpopulation, with fold change testing the difference in expression between two cell subpopulations. Genes with $P < 0.05$ were considered significantly differentially expressed genes (DEGs), where a log2-fold change < 0.25 indicated downregulated genes, and a log2-fold change > -0.25 represented upregulated genes.

Estimation of cell infiltration in DCM

The raw GSE141910, GSE1145, GSE116250, and GSE116250 datasets were downloaded from the GEO database, which includes detailed information such as platform, sample, and phenotypic data. The obtained raw gene expression values were log2 transformed.

The xCell [18], CIBERSORT [19], EPIC [20], and MCP-counter [21] algorithms were used to estimate the degree of cell infiltration. xCell is a robust algorithm that can be used to analyzes the infiltration levels of 64 immune and stromal cell types. CIBERSORT is a tool used for the deconvolution of the transcriptome expression matrix based on the principle of linear support vector regression. The estimating the proportion of immune and cancer cells (EPIC) algorithm as a method can estimate the proportions of immune and cancer cells. In addition to gene expression data were utilized, support vector regression (SVR) was used to calculate the proportions of each cell type. The microenvironment cell populations counter (MCPcounter) algorithm was performed to estimate the abundance of different cell types within tissues based on the gene expression characteristics of immune and non-immune cell types using a linear regression model.

Moreover, single-sample gene set enrichment analysis (ssGSEA) as a commonly used method for immune cell infiltration analysis was applied to estimate the relative abundance of macrophage subpopulations. By this method, we compared the gene expression data of each sample with a specific gene set to estimate the relative enrichment level of this gene set in the sample. Specifically, we used ssGSEA to sort all genes based on their expression levels from high to low and calculated the cumulative distribution function of genes with higher expression levels within a gene set, thus resulting in a cumulative distribution function called the gene set enrichment score (GSE). Then, the expression levels of all genes in each sample were sorted from high to low, and the gene set enrichment score corresponding to each position was calculated. Finally, the scores at these positions were averaged or weight averaged to obtain the ssGSEA score of the sample on the gene set, which was used to estimate the relative abundance of the immune cell type in the sample.

Developmental trajectory inference

We explored the differentiation trajectories of the selected clusters by the monocle package (version 2.22.0) in R (version 4.2.2), and separated the interesting cell clusters using the "subset" command of Seurat. Then we performed the "newCellDataSet" function to construct a CellDataSet object, and further filtered out low-quality cells and genes, with the "min_expr" parameter set to 0.1. through the "detectGenes" function and the "subset" function, which was accomplished after calculating the size factors and estimating the dispersions. Two thousand highly variable genes were finally selected, and then reduced for dimensionality by "reduceDimension" function with the "DDRTree" method. The DDRTree method was utilized to infer the pseudotime trajectory of cells. By combining the differentiation status of cell subpopulations with the pseudotime trajectory of cells, the degree of differentiation of cell subtypes was determined. The functions "plot_cell_trajectory", "plot_genes_in_pseudotime", and "plot_genes_branched_heatmap" were used for visualization.

CytoTRACE as a computational method for predicting cell differentiation status based on single-cell RNA sequencing data (https://cytotrace.stanford.edu/) was applied to analyze the differentiation status of fibroblasts, T cells, NK cells and myeloid cell subpopulations. The functions "plotCytoGenes" and "plotCytoTRACE" were also used for visualization.

Tissue preference of cell types

To quantify the distribution of cell types across tissues (normal and DCM samples), we used the R package sscVis (v.0.1.0) to calculate the odds ratio (OR) to indicate preference [22]. Fisher's exact test was performed on the contingency table to obtain OR values and corresponding p values. An $OR > 1.5$ indicates that the cell type is more likely to be distributed in the tissue sample, while an $OR < 0.5$ represents that the cell type is less likely to be distributed.

SCENIC analysis

We used the single-cell regulatory network inference and clustering (SCENIC) method to identify regulatory modules and their potential targets. The main process consists of three parts, in which we used the GRNBoost2 method to infer co-expression modules, and then applied the RcisTarget function to identify modules with significantly enriched motifs for correcting upstream regulatory factors while also eliminating indirectly targeted genes lacking motif support. Finally, we evaluated the activity of the regulatory modules at single-cell resolution by using the "AUCell" function. The SCENIC analysis pipeline was implemented through Python tools to obtain data on human upstream and downstream 10 kb motifs from the cisTarget database (hg38_10kbp_up_10kbp_down_full_tx_v10_clust.genes_vs_motifs.rankings.feather) and transcription factor motif data (motifs-v9-nr.hgnc-m0.001-o0.0.tbl). A total of 1839 transcription factor motifs were inputed, and then the "CalcRSS" function in the R package SCENIC (v.1.2.4) was applied to identify cell-specific regulatory activity scores (RSS) for the regulatory modules.

Functional enrichment analysis

Differential expression analysis was performed with the "FindAllMarkers" function in the Seurat package with default parameters. Genes with an adjusted $P < 0.05$ and $|\log_2 FC| > 0.25$ were considered significantly DEGs. Gene set enrichment analysis (GSEA) was used to assess pathway enrichment status. All enrichment analyses were conducted using the clusterProfiler package (version 4.0.1).

Metabolic activity scores at single-cell resolution

The R package scMetabolism (v0.2.1) was used to visualize and quantify the metabolic activity of individual cell within each cell cluster. Metabolism-related gene sets were obtained from Kyoto Encyclopedia of Genes and Genomes(KEGG), REACTOME, the molecular signatures database (MsigDB; https://www.gsea-msigdb.org/gsea/msigdb/human/collections.jsp#H), the FerrDb database (http://www.zhounan.org/ferrdb/current/), and the human autophagy database (HADb; http://www.autophagy.lu/index.html). Metabolic activity scores were calculated using the ssGSEA, AUCell, VISION, and GSVA algorithms. Finally, the metabolic activity of different pathways in different cell types was evaluated to identify pathways with significant differences. In this study, we applied AUCell method to analyzing the REACTOME metabolic genome.

Cell–cell communication

Cell communication can trigger a series of physiological and biochemical changes occur within the target cell through cell signal transduction, ultimately manifesting as the overall biological effects of the target cell. Intercellular communication mediated by the interaction between cell surface ligands and receptors reveals the association of various cell types during development, which is crucial in various biological processes. To detect the interactions between different cell types, we used the "CellChat" package (v.1.6.1) in R to predict the key signal inputs and outputs of cells, as well as the interactions between these cells and signals since CellChat is based on the gene expression profiles of ligands and receptors

in different cell types to infer their interactions and construct a cell communication network.

Statistics

Statistical analyses were performed using R (version 4.2.2) and Python (v.3.7.8). All figures were generated using R Studio. Comparisons between groups were conducted using χ^2 tests and Fisher's exact test for categorical variables. Wilcoxon rank-sum tests and Kruskal–Wallis tests were used for continuous variables. $P > 0.05$ were considered not statistically significant. In GSEA, p values were also adjusted based on the false discovery rate (FDR) for multiple hypothesis testing. Unless otherwise noted, each experiment was repeated three or more times with biologically independent samples.

Results

Profiling the single-cell transcriptomic landscape of the left ventricle

To more precisely describe the cellular landscape within the left ventricle of the heart, 2 scRNA-seq datasets, GEO183852 and GEO145154 with totaling 85,927 cells, were analyzed. The DCM patient clinical data are shown in Additional file 7: Table S1. PCA of pseudobulk data indicated that sex and age had no effect in this population. (Additional file 1: Fig. S1A). ScRNA-seq data from the index two sets of data were merged and clustered with the Seurat R package using both CCA and PCA based methods. Following rigorous quality control and clustering analysis, we obtained a total of 70,958 cells and 23 clusters with distinct expression features (Additional file 1: Fig. S1B), comprising 3 normal heart samples and 7 DCM samples (Additional file 1: Fig. S1C). The cell clusters were manually annotated based on the marker genes of each cell type, and 9 cell types were identified, including fibroblasts, endothelial cells, myeloid cells, pericytes,

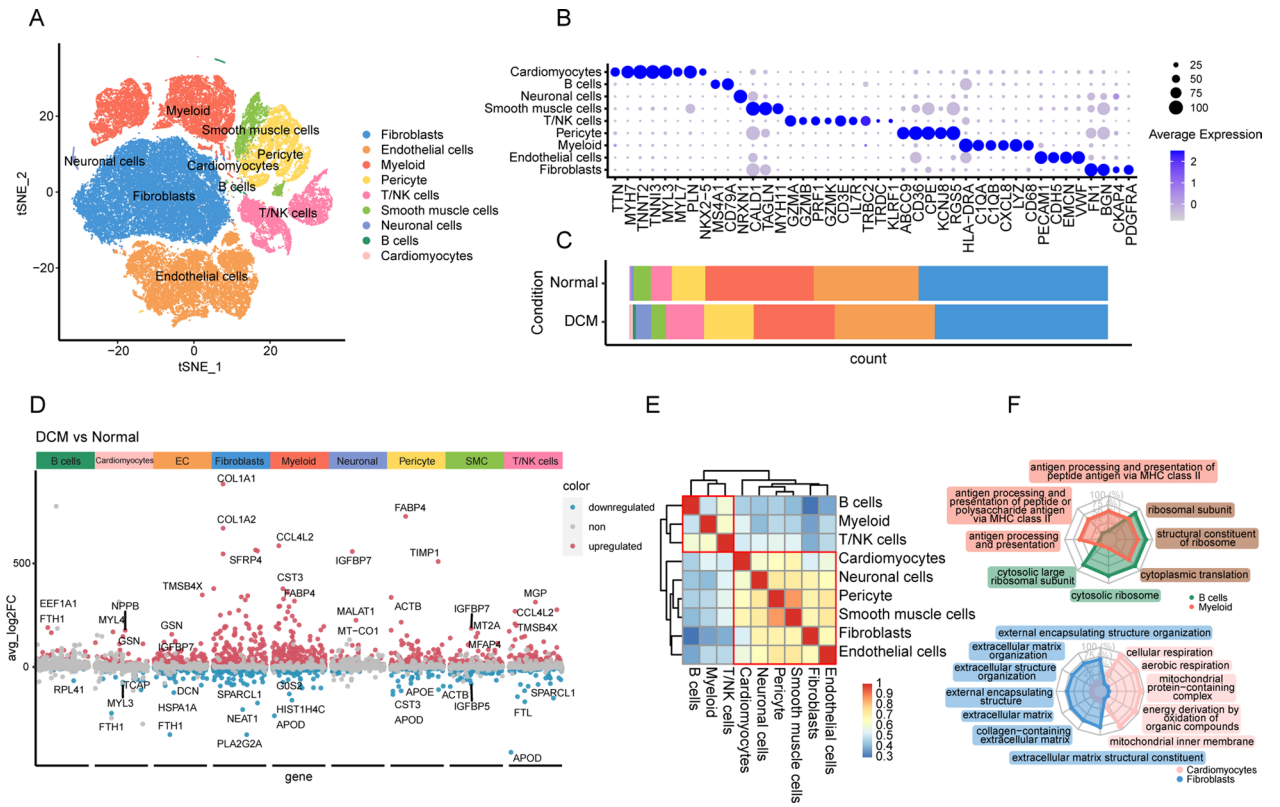

Fig. 1 Landscape of DCM and normal samples based on single-cell data. **A** t-SNE plot displaying 70,958 cells from DCM and normal samples. **B** Dot plot showing the proportional expression levels of typical markers used for identifying each cell type. The color key from gray to purple represents low to high expression levels. The size of the dots represents the percentage of cells expressing the gene. **C** Distribution of cell subtypes in DCM and normal samples. **D** Differential genes in each subtype between DCM and normal samples. Red represents upregulated genes, and blue represents downregulated genes. Genes with $P < 0.05$ and $\log_2$ fold change > 0.25 were considered significantly upregulated, while genes with $P < 0.05$ and $\log_2$ fold change < -0.25 were considered significantly downregulated. **E** Spearman correlation analysis between cell types. **F** Functional comparison of biological processes between B cells and myeloid cells (upper) and between cardiomyocytes and fibroblasts (lower)

T/NK cells, smooth muscle cells, neuronal cells, B cells, and cardiomyocytes (Fig. 1A, B). We found that neuronal cells, B cells, and T/NK cells were more likely to be expressed in DCM, while cardiomyocytes and myeloid cells were shown to be markedly expressed in normal samples (Fig. 1C, Additional file 1: Fig. S1D) based on OR analysis. Subsequently, the purity of the cell populations in all the samples was calculated using ROGUE, which shown that myeloid cells, fibroblasts and T/NK cells exhibited with high heterogeneity (Additional file 1: Fig. S1E). The differential expression of genes across different cell types was strongly influenced by the disease state (Fig. 1D, Additional file 7: Table S2), particularly in fibroblasts and myeloid cells. Significant genes for each cell subtype, including *LUM*, *VMF*, *IL1B*, *RGS5*, *NKG7*, *MYH11*, *GPM6B*, *IGLC2*, and *ACTA1*, are shown in Additional file 1: Fig. S1F. Additionally, the top 20 significant DEGs in each cell type are obtained (Additional file 1: Fig. S1G and Additional file 7: Table S3). Spearman correlation analysis revealed cell type-specific transcriptional profiles for both immune and non-immune cells (Fig. 1E). B cells had less correlation with myeloid cells within immune cells, each exhibiting distinct transcriptional features. Among non-immune cells, smooth muscle cells were more strongly correlated with pericytes, while cardiomyocytes shown a weak correlation with fibroblasts. This results are attributed to the developmental processes of DCM, indicating fibroblasts with independent of immune cells and cardiomyocytes. On the other hand, analysis with GSEA revealed the distribution features of different cells in physiological activities, such as B cells and T cells specific enrichment in cellular component-related processes, cardiomyocytes mainly in cellular respiration and aerobic respiration, fibroblasts involved in positive regulation of leukocyte activation and immune response regulatory signaling pathways, and myeloid cells correlated with extracellular matrix and ribosomal structure molecular functions. Compared to myeloid cells, B cells are enriched in large ribosomal subunit and ribosome cellular components, while myeloid cells are more existed in functions related to antigen processing and presentation via MHC class II peptides. Fibroblasts were more involved in extracellular matrix organization and other biological functions than cardiomyocytes, while cardiomyocytes were more related to cellular respiration, aerobic respiration, and other biological processes (Fig. 1F).Taken together, there is both correlation and heterogeneity among cell types in DCM, in which B cells show significantly different transcriptional features than other immune cells, while fibroblasts exhibit more distinct features than immune cells and cardiomyocytes. Given that the cardiac microenvironment also plays a crucial role in DCM that may influence the response to immunotherapy, we here utilized bulk-seq data from GSE141910 and data from van Heesch et al. (HubnerLab database) [23] on dilated cardiomyopathy to further analysis.(Additional file 7: Table S1). By quantified the proportions of immune cells in cardiac tissue and detected the changes in immune subtypes and non-immune cell subtypes in DCM patients, we found that most cell types were significantly different between DCM and normal cardiac tissues. For example, fibroblasts, B cells, T cells, endothelial cells and NK cells were significantly increased in DCM, but macrophages shown a significant decrease (Additional file 2: Fig. S2A-E). To understand the alternations in the cellular composition in DCM, we next meticulously analyze the changes in fibroblasts, T/NK cells and myeloid cells in DCM at single-cell level.

Dissection and clustering of fibroblasts in DCM

Cardiac fibroblasts as the dominant cell type in the heart [24] undergo phenotypic changes during cardiac remodeling, in which they acquire a myofibroblast character, proliferate and produce extracellular matrix proteins, thereby maintaining the structural integrity of the injured heart. Here, we identified eight subpopulations within 26,435 fibroblasts, including F0, F1, F2, F3, F4, F5, F6, and F7 (Fig. 2A), among them, the F1, F2, F3, F5, F6, and F7 cell subpopulations have uniquely high-expressing genes. The top 10 significantly expressed genes in the cell subpopulations are shown in Additional file 3: Fig. S3A and Additional file 7: Table S4. In F1, *DLK1*, a non-classical Notch ligand that regulates the Notch signaling pathway and *SMOC2* were highly expressed [25]. *DLK1* is involved in embryonic development and adult cell differentiation and negatively regulates the differentiation of cardiac fibroblasts into myofibroblasts, thereby controlling myocardial fibrosis [26]. On the other hand, *SMOC2* exhibited high expression during embryonic development and wound healing, thus being potential as a target for controlling tumor growth and vascular generation in myocardial ischemia [27, 28]. In F2 subpopulation, *IGFBP6* and *FGFBP2* are highly expressed. *IGFBP6* has been shown to play a role in the positive regulation of cell migration and stress-induced MAPK cascade activation, serving as a biomarker for breast cancer, carcinoma in situ, and leiomyomas. *FGFBP2* encodes a member of the fibroblast growth factor-binding protein family, and its protein is selectively secreted by cytotoxic lymphocytes and may participate in cytotoxic lymphocyte-mediated immunity. In F3, *POSTN*, *THBS4*, and *CLU* were highly upregulated. Overexpression of *POSTN* can lead to cardiac dysfunction and increase the risk of cardiac fibrosis [29]. *THBS4* is an adhesive glycoprotein that mediates cell–cell and cell–matrix interactions and participates in various

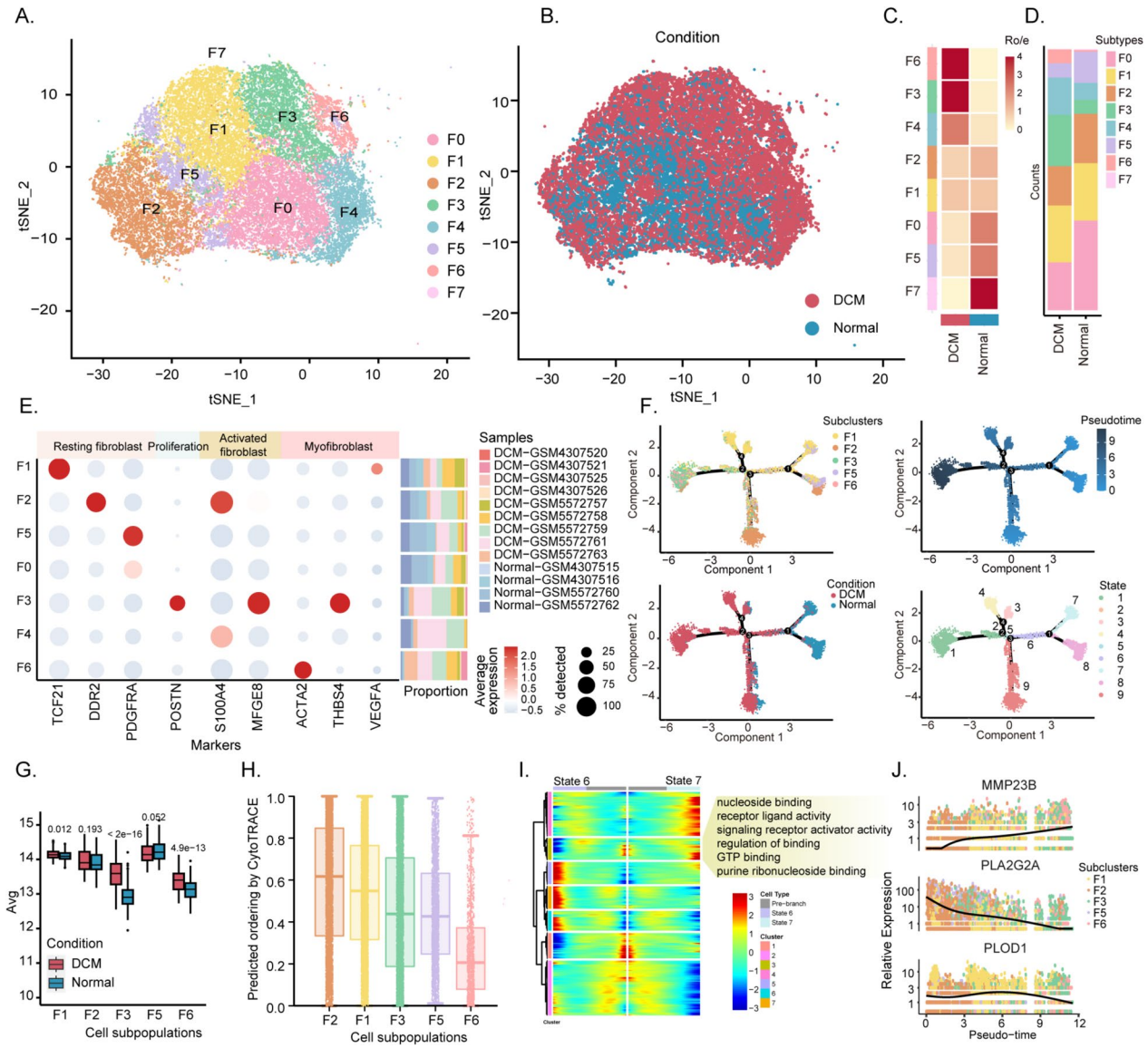

Fig. 2 Landscape and features of fibroblasts in DCM and normal samples. **A** t-SNE plot displaying 26,435 fibroblasts. **B** t-SNE plot displaying the distribution of fibroblasts in DCM and normal samples. **C** Preference of tissue morbidity rates estimated by Ro/e scores for each fibroblast type. Ro/e > 1 indicates a significant preference for the tissue. **D** Distribution of fibroblast subtypes in DCM and normal samples. **E** Dot plot showing the expression levels of fibroblast state markers used to identify each subtype. **F** Top left, pseudotime trajectory of six fibroblast subtypes; top right, pseudotime trajectory of six fibroblast subtypes with pseudotime; bottom left, distribution of DCM and normal samples in the pseudotime trajectory of six fibroblast subtypes; bottom right, cell state of the pseudotime trajectory of six fibroblast subtypes. **G** Infiltration levels of fibroblast subtypes in DCM and normal samples calculated based on deconvolution methods. **H** CytoTRACE analysis of the differentiation potential of fibroblast subtypes. **I** Left, heatmap depicting differentially expressed genes in fibroblasts based on the pseudotime trajectory; blue to red represent low to high expression patterns, respectively; right, GO analysis for Cluster 3. **J** Dynamic expression of differentially expressed genes within pseudotime. The data were sorted based on pseudotime

processes, including cell proliferation, migration, adhesion, attachment, inflammatory response to central nervous system injury, regulation of vascular inflammation, adaptation of the heart to pressure overload, myocardial function, and remodeling. However, *THBS4* overexpression induces fatal cardiac atrophy [30]. *CLU* is a secretory chaperone that can also be found in cytoplasmic solutes under certain stress conditions, and associates with several basic biological events, such as cell death, tumor progression, and neurodegenerative diseases, showing an important role in cell proliferation [31]. F3 may represent a subpopulation characterized by cell proliferation. *FGF7*

highly expressed in F5 has been proved to exert roles in various biological processes, including embryonic development, cell growth, morphogenesis, tissue repair, tumor growth, and invasion, which is also associated with the apoptosis pathway of synovial fibroblasts and the GPCR pathway [32]. Compared to that in normal tissue, *FGF7* is downregulated in pathological human cardiac tissue [33]. GPC3 is also upregulated in F5, which has been showed to play a role in regulating cell division and growth control. Several molecules such as *ELN*, *ACTA2*, *APOE*, and *COL1A1* were detected with high expression in F6. Among them, the *ELN* encodes a protein as one of the components of elastic fibers that might involve in increase of elastic protein synthesis in adult patients with myocardial injury [34, 35]. Other proteins also implicated important biological processes such as vascular contraction, blood pressure homeostasis, cardiovascular aging [36–38], and fibrosis. F7 subpopulation shown an upregulation of *ZBP1* that as a pattern recognition receptor actively regulates inflammation in response to mtDNA in inflammatory cells, fibroblasts, and endothelial cells [39].Moreover, fibroblast subpopulations also distributed differently between DCM and normal samples (Fig. 2B). Using the Ro/e method, we quantified the preference of each subpopulation for DCM samples versus normal samples based on the ratio of observed to expected cell numbers (Fig. 2C), and found that samples from DCM patients were more abundant in subpopulations F3, F4 and F6, suggesting the potential involvement of these subpopulations in DCM. Figure 2D shows that the proportion of F0-F6 fibroblast subpopulations are higher than that of the F7 subpopulation in both DCM and normal samples. The marker genes for fibroblasts in different states have been identified [4, 40] (Fig. 2E). We here observed significant upregulation of the resting markers *TCF21*, *DDR2*, and *PDGFRA* in F1, F2, and F5, indicating that the majority of fibroblasts in these three subpopulations were in a quiescent state. Additionally, the activated marker *S100A4* was also significantly upregulated in F2, making the subpopulation of fibroblasts in an activated state. F3 displayed high expression of the proliferation marker gene *POSTN* with activation of *THBS4* and *MFGE8*, which enhanced the phagocytosis of apoptotic cells. Thus, the F3 cell subpopulation is in cell state transition in progress. The upregulation of *ACTA2* and *VEGFA* in F6 indicated that most cells in these subpopulations are myofibroblasts, representing the cellular state in the late stages of myocardial injury. Taken together, fibroblast subpopulations F1, F3 and F6 were significantly abundant in DCM samples than in normal samples, as validated across bulk-seq samples (Fig. 2G).

Functional analysis of the fibroblast subpopulations revealed that F1, F2, and F6 were enriched mainly in cellular component-related processes (Additional file 3: Fig. S3C, D), and F3 was primarily related to molecular functions of extracellular matrix structure, heparin, and glycosaminoglycan binding. F5 was mainly presented in biological processes such as complement activation, alternative pathways, complement and coagulation cascades, and complement-dependent cytotoxicity, while F7 participated in antigen processing and the presentation of exogenous peptide antigens via MHC class II. These results suggest that different cellular subpopulations may exert distinct influence on the composition and function of fibroblasts. Therefore, we here identified several fibroblast subpopulations expressing genes related to cell proliferation, cytotoxicity, immunity, and fibrosis that execute different functions with distinct states in DCM. Our findings provide new insights into the pathogenesis of DCM.

Trajectory analysis of fibroblast subpopulations

To further understand the dynamic transcriptional changes, the pseudotime developmental trajectory analysis was carried out with F1, F2, F3, F5 and F6 fibroblast subpopulations. (Fig. 2F). The F2 cell subpopulation is positioned at the forefront of other subpopulations, while the F1, F3, and F5 cell subpopulations are relatively located in the middle, and the F6 cell subpopulation is mainly distributed at the end, which is consistent with previous observations. Relatively, the F2 cell subpopulation have higher differentiation potential, while the F6 cell subpopulations have lower differentiation potential (Fig. 2H).

At branch point 1, which is mainly driven by the F2 cell subpopulation, we found that Cluster 3 genes are highly expressed in State 6 cells and weakly expressed in State 7 cells and are strongly enriched in nucleotide binding, receptor ligand activity, signaling receptor activator activity, and GTP binding functions (Fig. 2I, Additional file 7: Table S5). In State 6, DCM samples are predominant, while in State 7, normal samples are predominant. At branch point 2, F3 was mainly distributed in State 1, where Cluster 1 genes were highly expressed in State 1 cells but weakly expressed in State 2 cells. These genes were enriched in collagen-containing extracellular matrix and focal adhesion, as well as involved in extracellular matrix organization and other biological processes, indicating strong cell migration ability in State 1 cells (Additional file 3: Fig. S3B). Conversely, Cluster 3 genes, which are involved in cotranslational protein targeting to membrane, nuclear-transcribed mRNA catabolic process, nonsense-mediated decay, and other biological processes, are expressed with low levels in State 1 cells but upregulated in State 2 cells (Additional file 7: Table S6).

Among the DEGs of cell subpopulations, *MMP23B* expression depended on cell state, while *PLA2G2A* and *PLOD1* expression shown an opposite trend of the cell state (Fig. 2J, Additional file 7: Table S7). Previous studies have shown that *PLA2G2A* mutations mediate coronary heart disease, and *PLOD1* can stabilize collagen during the fibrosis process [41]. All of the results indicate that fibroblast subpopulations in DCM exhibit strong cell migration ability, which may explain the interaction between fibroblasts and other cells in DCM.

Distribution and characteristics of T cells and NK cells in DCM

T cells and NK cells (n = 4865) are common populations in DCM patients. Using the Seurat package in R, we reclustered T cells and NK cells (Fig. 3A), and characterized CD4 + and CD8 + T cell subgroups in DCM patients using known T cell marker genes (CD4 and CD8A) and functionally identified cell subpopulations (Fig. 3B, C, Additional file 4: Fig. S4A). We revealed 16 clustered subpopulations, including 2 CD4 + T cell subpopulations (CD4-C1-CDKN1A, CD4-C2-RGS1), 7 CD8 + T cell subpopulations (CD8-C1-HSPA1B, CD8-C2-FGFBP2, CD8-C3-GZMK, CD8-C4-FGFBP2, CD8-C5-FABP4, CD8-C6-XCL1, and CD8-C7-STMN1), 2 NK cell subpopulations (NK1 and NK2), 1 naive T cell subpopulation, and other T cell-like subpopulations (MONO, FIB1, FIB2, and DC). Based on the Ro/e index, CD4-C1-CDKN1A (CD4 Tfh), CD8-C6-XCL1 (CD8 Trm1), and CD8-C2-FGFBP2 (CD8 Tem1) cells were preferentially distributed in DCM, but CD8-C7-STMN1 (CD8 Trm2) T cells were not there (Fig. 3D, E). Figure 3F and Additional file 7: Table S8 show the top 10 significantly upregulated genes in each T cell subpopulation. To our knowledge, the CD4-C1-CDKN1A (CD4 Tfh) cell subpopulation has not been previously reported in similar studies. We found that the infiltration of the CD4-C1-CDKN1A (CD4 Tfh) cell subpopulation was upregulated in DCM (Fig. 3G). Among the highly expressed genes in DCM (Fig. 3H), *CDKN1A* is associated with proteasome-mediated degradation in regulating the activated PAK-2P34 signaling pathway, which is involved in ubiquitin-protein ligase binding and cell cycle protein binding functions. *CCR6* as a receptor has been shown to be crucial for B cell maturation and antigen-driven B cell differentiation, regulating T cell migration and recruitment in inflammatory and immunological response processes. *CREM* encodes different transcripts, as transcriptional activators or repressors, are important component of cAMP-mediated signal transduction. *LMNA*, encoded a protein of the inner nuclear membrane, is one of the most commonly mutated genes associated with DCM [42, 43]. Additionally, the upregulation genes in the CD4-C1-CDKN1A (CD4 Tfh) cell subpopulation also participate in the regulation of activated T cells, cytokines, adhesion molecule binding, and other biological processes (Fig. 3J, Additional file 7: Table S9). These data suggest that CD4-C1-CDKN1A may have a significant impact on the composition and function of T cells.

Next, we conducted pseudotime trajectory analysis separately for CD4 + T cells to further understand the immunodynamics. The trajectory of CD4 + T cells revealed that CD4-C2-RGS1 (CD4 Trm) cells are located at the opposite end of CD4-C1-CDKN1A (CD4 Tfh) cells (Additional file 4: Fig. S4B). By CytoTRACE, we predicted that CD4-C1-CDKN1A (CD4 Tfh) cells might have greater differentiation potential, while CD4-C2-RGS1 (CD4 Trm) cells were weak on that (Additional file 4: Fig. S4B). At branch point 1, the CD4-C1-CDKN1A cell subpopulation could differentiate into CD4-C1-CDKN1A and CD4-C2-RGS1 cell subpopulations, where Cluster2 genes were upregulated in State2, but kept at a low level in State5. These genes were mainly involved in cytosolic ribosomes, cotranslational protein targeting to membranes or to ER, nuclear-transcribed mRNA catabolic processes, and nonsense-mediated decay. Inversely, Cluster 3 genes were expressed at low levels in State2 and unregulated in State5, and enriched in the T cell receptor complex, plasma membrane signaling receptor complex, immunological synapse, and ficolin-1-rich granule (Additional file 4: Fig. S4C, Additional file 7: Table S10). At branch point 2, the CD4-C2-RGS1 cell subpopulation differentiated into two different branches, indicating heterogeneity within the cell subpopulation (Additional file 4: Fig. S4D). Among them, the Cluster 2 gene set was upregulated in State 3, but downregulated in State 4, involving in many biological processes such as response to glucocorticoids, corticosteroids, cAMP, organophosphorus and steroid hormones, which provided clear annotations of the heterogeneity in the CD4-C2-RGS1 cell subpopulation (Additional file 7: Table S11). On the other hand, the expression of *PTPRCAP* and *RPS26* gradually decreased with changes in the cell state. *PTPRCAP* is associated with the transmembrane phosphoprotein specific to the tyrosine phosphatase PTPRC/CD45 that is a key regulatory factor for the activation of T and B lymphocytes. *TXNIP* was increased with changes in cell state (Additional file 4: Fig. S4E) for *TXNIP*-related pathways, including inflammasome and gene expression pathways, that might exert protective effects against cardiac damage when mutated [44]. Moreover, CD8-C1-FGFBP2 (CD8Tem1) was upregulated in DCM (Fig. 3G). Among the highly expressed genes (Fig. 3I), *FGFBP2* encodes a protein secreted selectively by cytotoxic lymphocytes into serum that participates in immune responses

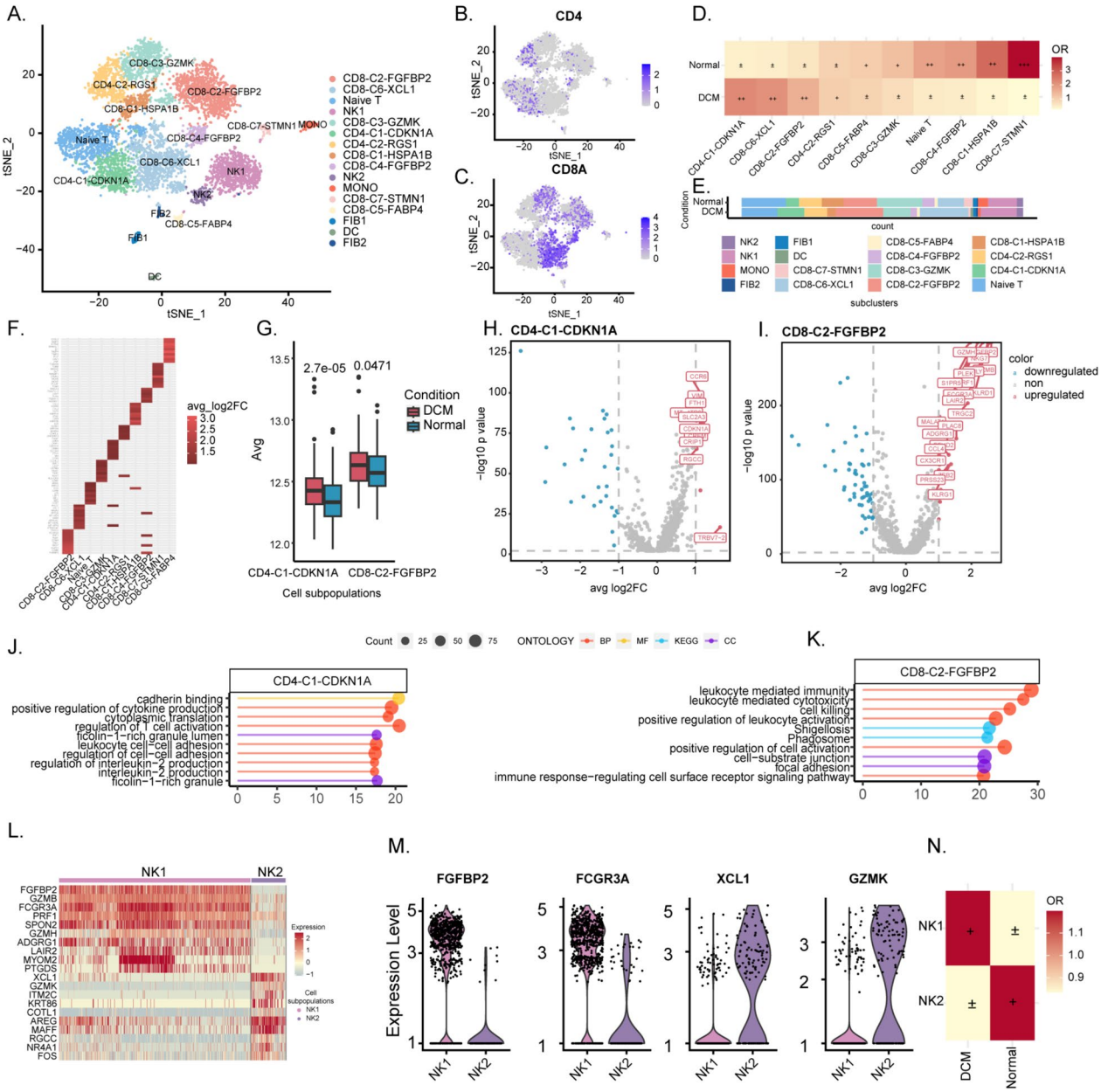

Fig. 3 Landscape and features of T cells and NK cells in DCM and normal samples. **A** t-SNE plot displaying 4865 T cells and NK cells. **B**, **C** Feature plots showing the expression of canonical cell marker genes used to define CD4 + cells and CD8 + cells. **D** Heatmap showing the tissue morbidity rates estimated by Ro/e scores for each cell type. **E** Distribution of cell subtypes in DCM and normal samples. **F** Mean differential gene expression values for each cell subtype. The color scale from black to red indicates increasing significance of differential expression. **G** Infiltration levels of T cell subtypes in DCM and normal samples calculated based on deconvolution methods. Red represents DCM, blue represents normal samples, and $P < 0.05$ indicates significant difference. **H** Significantly differentially expressed genes in the CD4-C1-CDKN1A subtype compared to the other subtypes. Red indicates upregulation relative to other subtypes, and blue indicates downregulation. Rows represent the mean fold change, where a log2 fold change > 1 indicates upregulation and < 1 indicates downregulation. Columns represent the significance of subgroup differences calculated by t tests, where $P < 0.05$ indicates significant difference. **I** Similarly, significantly differentially expressed genes in the CD8-C2-FGFBP2 subtype compared to the other subtypes were identified. **J** Enriched functions and pathways associated with the top 10 genes in the CD4-C1-CDKN1A subgroup. **K** Enriched functions and pathways associated with the top 10 genes in the CD8-C2-FGFBP2 subgroup. **L** Heatmap showing the top 10 DEGs between the NK1 and NK2 subtypes. **M** Distribution of significantly highly expressed genes in the NK1 and NK2 subtypes. **N** Preference of NK1 and NK2 subtypes in tissue estimated by Ro/e scores

mediated by cytotoxic lymphocytes. Another gene, *GZMB*, play a role to processe cytokines, degrade extracellular matrix proteins, and action related to chronic inflammation and wound healing. For *KLRD1*, an antigen primarily expressed on NK cells, is classified as a type II membrane protein due to its external C-terminus that mediates cytotoxic activity and cytokine secretion upon immune stimulation. CD8-C1-FGFBP2 (CD8Tem1) is preferentially distributed in DCM, mainly participating in focal adhesion, indicating its role in cell migration (Fig. 3K, Additional file 7: Table S9).

The prediction using CD8 + T cells trajectory and pseudotime analysis shown that the CD8-C5-FABP4 (CD8 Tem4) and CD8-C6-XCL1 (CD8 Trm1) cell subpopulations were greater potential in differentiation (Additional file 4: Fig. S4F), compared with the CD8-C2-FGFBP2 (CD8 Tem1) cell subpopulation. Generally, CD8-C5-FABP4 (CD8 Tem4) differentiated into other CD8 + T cells at branch point 1, where Cluster5 genes were only upregulated in State3, and enriched in cell components and molecular functions such as cell killing, cytolysis, and defense response to fungus (Additional file 4: Fig. S4G and Additional file 7: Table S12). We found that the expression of the genes *RGS1*, *JUN*, *XCL1*, and *ZFP36L2* were significantly different between groups, and downregulated along with changes in the cell state, but the expression of *TXNIP* and *GNLY* shown an opposite trend. Both *RGS1* and *XCL1* related pathways involve downstream signaling by GPCRs, thus playing important roles in leukocyte trafficking and vascular inflammation (Additional file 4: Fig. S4H).

The lineage structure of T lymphocytes in the left ventricular environment of DCM patients was inferred through developmental trajectory analysis, which revealed a unique lineage landscape. The results suggest that the presence of these inflammation-related genes are highly expressed in the late stage of the cell state. For example, *TXNIP* expression level was increased in CD4 + and CD8 + cells, indicating its role in DCM.

NK cells are generally divided into CD56bright and CD56dim NK cell subpopulations, where CD56dim NK cells show cytolytic activity, and CD56bright NK cells can differentiate into CD56dim NK cells through expressing *CD16*, *PEN5*, and *CD57* [45]. We detected the top 10 significant DEGs in the NK1 and NK2 cell subpopulations in DCM (Fig. 3L and Additional file 7: Table S13), with specific upregulated or downregulated genes (Additional file 4: Fig. S4I). For NK cell subpopulations (n = 953), NK1 cell subpopulations were mainly distributed in DCM (Fig. 3N), with unique expression of FGFBP2 (Fig. 3M, Additional file 4: Fig. S4J) that participated in the immune responses mediated by cytotoxic lymphocytes. Other high-expressed genes in the subpopulation included *GZMB*, *PRF1*, *GZMH*, *FCGR3A*, *SPON2*, *CX3CR1*, and *PTGDS*, which implicated cytotoxicity and leukocyte-mediated immune processes, thus being defined as CD56dim NK cells (Additional file 4: Fig. S4K).However, NK2 is mainly distributed in normal cells (Fig. 3N), which expressed *XCL1*, a typical NK cell-related chemokine known to recruit conventional type 1 dendritic cells to the tumor microenvironment [46]. Another group of genes upregulated in the NK2 cell subpopulations was *ZFP36*, *ZFP36L2*, *PABPC1*, *XCL1*, *CXCR6*, *CXCR4*, *XCL2*, and *DUSP1*, which worked in the positive regulation of mRNA decay processes and the cellular response to chemokines, and other biological processes (Additional file 4: Fig. S4K, Additional file 7: Table S14), representing typical CD56bright NK cells. These results suggest that NK CD56dim cells are more highly expressed in the left ventricle of DCM patients.

Dissection and clustering of myeloid cells in DCM

As the most common population in DCM patients, myeloid cells (n = 11,908) were here reclustered in 11 infiltrating cell subpopulations (Fig. 4A, B) based on the expression levels of marker genes and functions (Fig. 4E), including 3 dendritic cell subpopulations, cDC-like1, cDC-like2, and cDC-like3, classical monocytes, 3 different types of macrophage subpopulations, M1-like, M2-like1, and M2-like2; and other myeloid-like subpopulations. The significant DEGs in the subpopulations were obtained(Fig. 4C, D and Additional file 7: Table S15). Then, using the Ro/e index, we revealed that dendritic cells were preferentially distributed in DCM, especially for cDC-like3 (Fig. 4F, G). cDC-like1 or cDC-like2 are involved in the positive regulation of cell activation and cell–cell adhesion (Fig. 4H), or actin filament organization and leukocyte migration (Fig. 4I), respectively. cDC-like3 could response to the molecules of bacterial origin, lipopolysaccharide, biological stimuli, and the TNF signaling pathway (Fig. 4J).

We also found that the monocyte subset Mono was mainly distributed in DCM patients (Fig. 4F, G), with overexpression of the genes *S100A8*, *S100A9*, and *S100A12* that were members of the S100 protein family related to the myeloid lineage and the action in resisting microbial infections and maintaining immune homeostasis. These proteins invade microbial pathogens required for metal nutrients in the host through "nutritional immunity" and directly inhibit the growth of pathogens. Also, they mediate receptors to initiate inflammatory signal transduction, induce cytokine expression, and participate in inflammatory reactions and immune regulation. Additionally, the increase of these proteins during pathological processes makes them available as biomarkers for screening and detecting related diseases [47]. Various

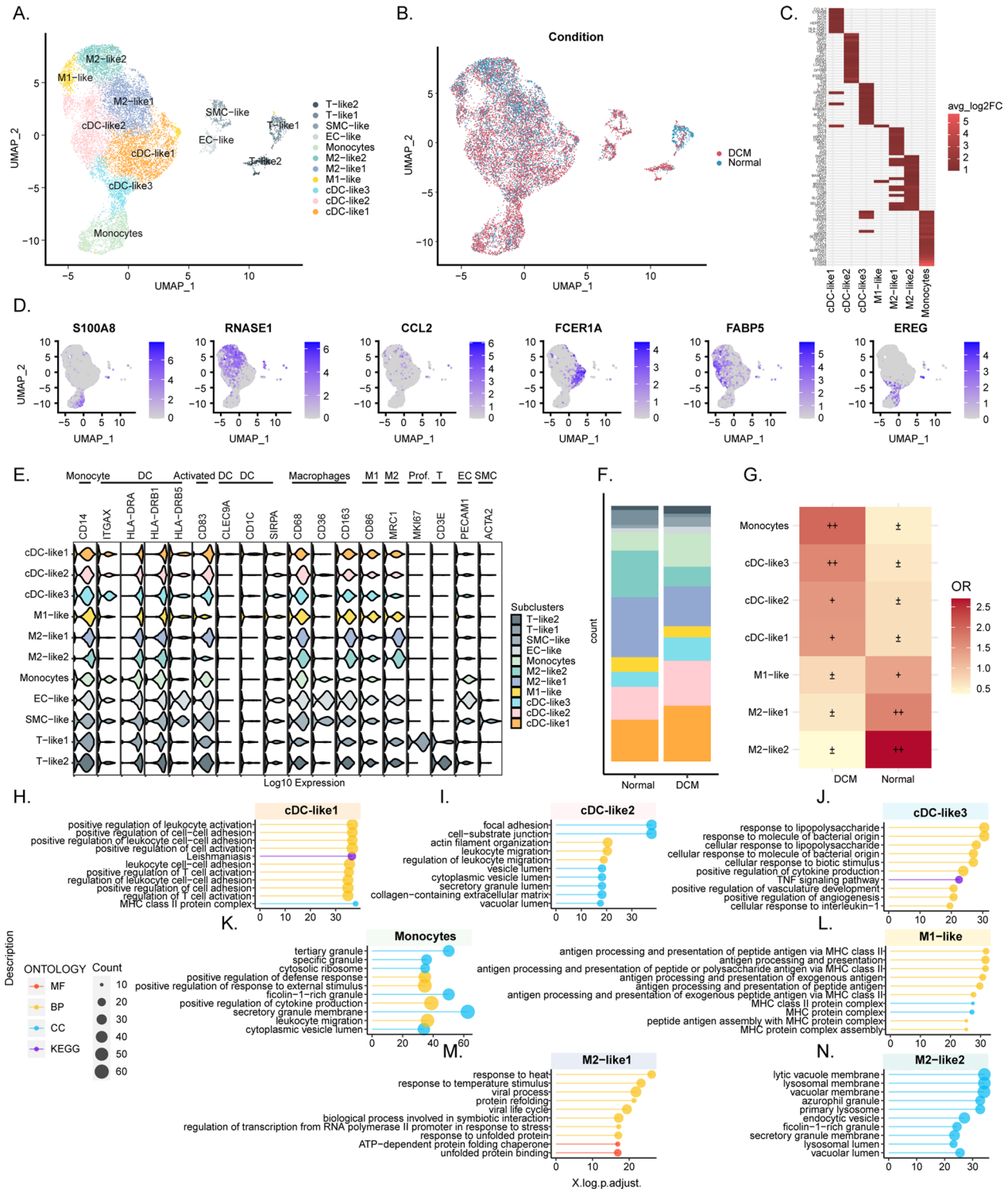

Fig. 4 Landscape and features of myeloid cells in DCM and normal samples. **A** t-SNE plot displaying 11,908 myeloid cells. **B** t-SNE plot showing the distribution of myeloid cells in DCM and normal samples. **C** Mean differential gene expression values for each cell subtype. The color scale from black to red indicates increasing significance of differential expression. **D** Feature plots showing the expression of canonical cell marker genes used to define each cluster. **E** Violin plots showing the proportional expression levels of typical markers used for identifying each cell type. **F** Distribution of myeloid cell subtypes in DCM and normal samples. **G** Preference of myeloid cell subtypes in tissue estimated by Ro/e scores. **H**–**N** Pathway and functional enrichment of the (**H**) cDC-like1, (**I**) cDC-like2, (**J**) cDC-like3, (**K**) Monocyte, (**L**) M1-like, (**M**) M2-like1 and (**N**) M2-like2 subpopulations

cellular components, such as the secretory granule membrane, tertiary granules, and ficolin-1-rich granules, were enriched in monocyte subtypes. Furthermore, monocyte subsets also related to regulation of cytokine production and defense responses, leukocyte migration and the response to external stimulus biological processes (Fig. 4K).

Two subtypes of macrophages, namely classically activated M1 and alternatively activated M2, harbor three subgroups, M1-like, M2-like1, and M2-like2. Ro/e analysis revealed that macrophages were generally abundant in normal samples, but M1 macrophages were more rich in DCM samples (Fig. 4F, G). In M1-like macrophages, these genes such as *FCER1A*, *TXNIP*, *CD1C*, *CD1E*, *CLEC10A*, *VSIG4*, *CTSH*, *YWHAH*, *HIST1H4C*, *HLA-DQA2*, *CPVL*, *FCGR2B*, and *CD9* (Fig. 4C) shown upregulation, which are involved in antigen processing and the presentation of peptide antigens via MHC class II and antigen processing and the presentation of exogenous antigens (Fig. 4L). In M2-like1, highly-expressed genes (Fig. 4C) play roles in responses to temperature stimuli, viral processes, protein folding, the viral life cycle, the regulation of transcription from the RNA polymerase II promoter in response to stress, and other biological processes, including *CCL2*, *SELENOP*, *JUN*, *EGR1*, *RNASE1*, *STAB1*, *FOS*, *F13A1*, and *IER2* (Fig. 4M Additional file 7: Table S16). M2-like2 macrophages with *MS4A4A* as a signature of M2 mainly expressed *RNASE1*, *FOLR2*, *DAB2*, *C1QA*, *LYVE1*, *LGMN*, *SELENOP*, *PLTP*, *SLC40A1*, *C1QC* and *C1QB* (Fig. 4C) in cellular components such as the lysosomal membrane, lytic vacuole membrane, primary lysosome, endocytic vesicle, and vacuolar lumen (Fig. 4N). It is essential to modulate macrophage activation to suppress inflammation by promoting the repolarization of proinflammatory (M1) macrophages toward anti-inflammatory (M2) macrophages. Compared to M1 macrophages, M2 macrophages are more plastic and easily repolarized to the inflammatory M1 state. Next, we explore the subtypes of M2 macrophages associated with DCM.

Identification of a novel M2 macrophage subpopulation associated with DCM

In DCM patients, the number of myeloid cells was generally less than that in normal individuals (Fig. 4G), which comes down to the samples in the late stages of DCM. Comparative analysis of two M2-like macrophages associated with DCM revealed that the genes highly expressed in M2-like1 were significantly enriched in response to topologically incorrect proteins and unfolded proteins, as well as in functions related to muscle tissue and organ development. The upregulated genes in M2-like2 were significantly enriched in antigen processing and the presentation of exogenous peptide antigens via MHC class II (Fig. 5A). To further evaluate the heterogeneity between these two M2-like macrophages, we analyzed the highly-expressed genes in M2 macrophages in normal cardiac tissue and DCM cardiac tissue (Fig. 5B). *CITED2* was detected with high expression in M2-like1 than in other subpopulations in DCM (Fig. 5B, Additional file 7: Table S17). Analysis of the functional annotations further revealed the involvement of *CITED2* in the regulation of transcription from the RNA polymerase II promoter in response to stress, myeloid cell differentiation, the regulation of DNA-templated transcription in response to stress, myeloid leukocyte differentiation, muscle organ development and the response to hypoxia (Additional file 7: Table S16). *CITED2* really regulates macrophage recruitment as an anti-inflammatory factor through cooperating with PPAR to induce the expression of anti-inflammatory genes by reducing the accumulation of HIF1a protein in macrophages and inhibiting the expression of pro-inflammatory genes [48]. In addition, other the highly-expressed genes in M2-like2 macrophages of DCM, such as *MARCK2*, *ALDHA1* and *TMEM173*, show anti-inflammatory functions, associated with cell migration [49], and promoting fibrosis and macrophage activation [50], respectively. Therefore, the M2-like2 subpopulation of macrophages exert crucial functions in inflammation inhibition and fibrosis promotion. We then used the non-overlapping upregulation genes in M2-like1 and M2-like2 as a signature gene set for M2 macrophage subpopulations to evaluate the scores in the samples by ssGSEA. Our results shown that M2-like1 was characterized by 192 genes, while M2-like2 by 323 genes. Validation in the GSE141910 and GSE1145 datasets further revealed that the M2-like2 subpopulation of macrophages is highly expressed in DCM, indicating that the subpopulation can be served as a key cell population for DCM (Fig. 5C).

To investigate the alterations in macrophage subpopulations in DCM, we performed pseudotime trajectory analysis on monocytes and macrophages to assess the potential differentiation relationships of macrophage subpopulations. The trajectory originated from monocytes, with M1 pro-inflammatory macrophages in the middle stage of differentiation and M2 anti-inflammatory macrophages in the late stage (Fig. 5D, Additional file 7: Table S18). CytoTRACE analysis indicated that monocytes shown the highest differentiation potential, compared with M2-like2 (Fig. 5E). M1 macrophages transformed into M2 macrophages at branch point 1, with more M2-like2 subpopulations exhibiting cell fate 2. Among the branch point in Cluster 3, genes related to SRP-dependent cotranslational protein targeting to the membrane, and the protein targeting to the ER were downregulated in cell fate 2 but upregulated in cell fate

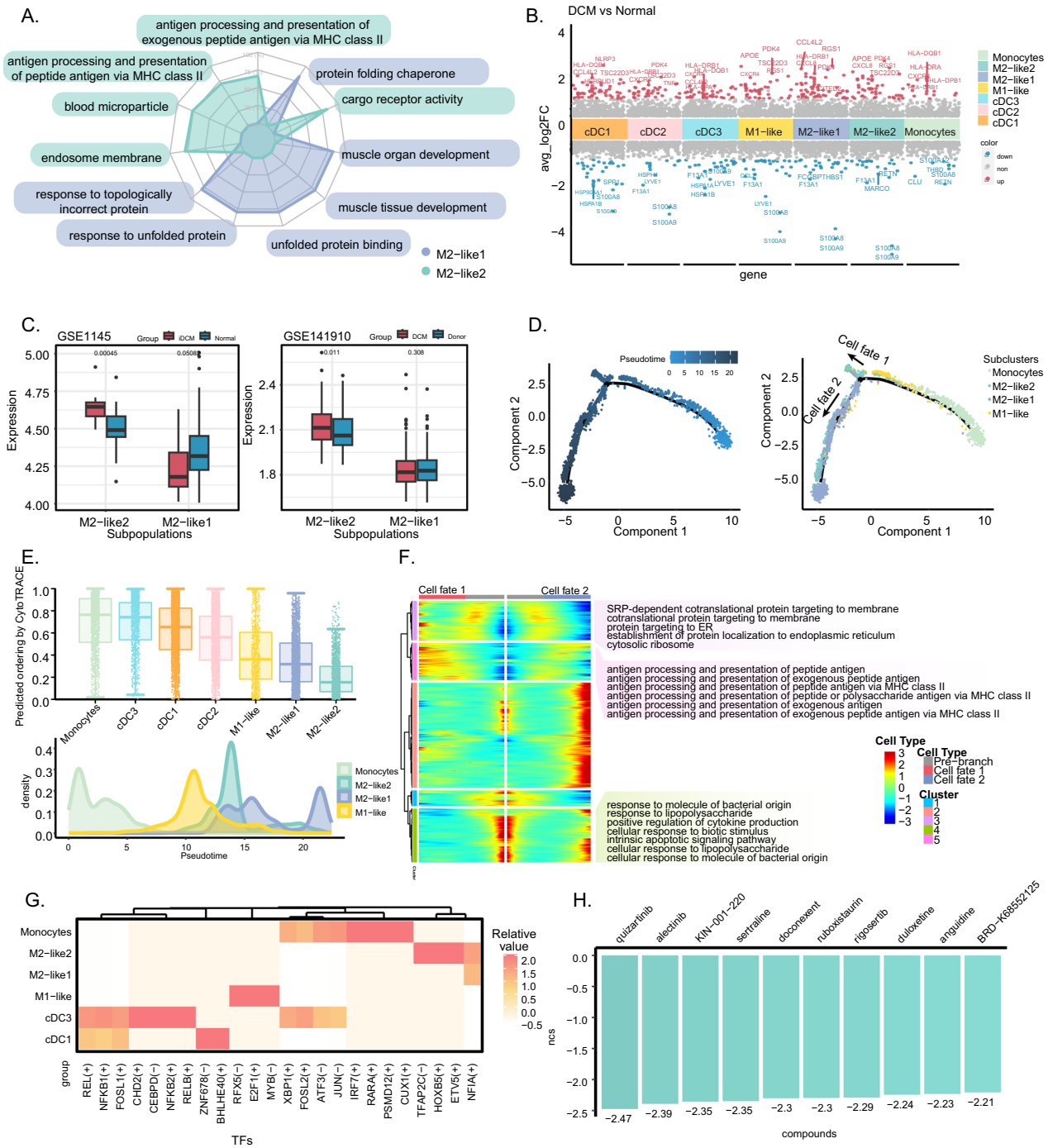

Fig. 5 Comparison of M2-like1 and M2-like2. **A** Comparison of the biological functions of M2-like1 and M2-like2. **B** Differential genes in myeloid cell subtypes between DCM and normal samples. Red represents upregulated genes, and blue represents downregulated genes. Genes with $P < 0.05$ and log twofold change > 0.25 were considered significantly upregulated, while genes with $P < 0.05$ and log twofold change < − 0.25 were considered significantly downregulated. **C** ssGSEA evaluation of M2-like1 and M2-like2 infiltration levels in the GSE1145 and GSE141910 bulk-seq datasets and comparison of infiltration levels between DCM and normal samples. **D** Pseudotime trajectory of monocytes and macrophages. **E** Top: CytoTRACE analysis of myeloid cell differentiation potential; Bottom: Pseudotime density distribution of monocytes and macrophages. **F** Differential gene modules and functions of cell fate 1 and cell fate 2 at branch point one. **G** Heatmap showing the levels of transcription factors in myeloid cells. **H** Top 10 compounds with negative similarity scores for drug-disease pairs. The x-axis shows the top 10 compounds with negative similarity scores for the drug–disease pairs. The y-axis shows the similarity scores of drug–disease pairs

1 (Fig. 5F), indicating that the functions of M2-like1 and M2-like2 macrophage subpopulations were changed during the occurrence of DCM.

Given different cell subpopulations involve distinct cooperative actions of transcription factors, we performed SCENIC analysis to identify the transcription factors associated with M2-like1 and M2-like2 cells (Fig. 5G). The transcription factors HOXB5, TFAP2C, ETV5, and NFIA were strongly correlated with the M2-like2 cell subpopulation, while NFIA was tightly associated with M2-like1, which has been proved as a risk factor for heart failure[51]. Moreover, HOXB5 or TFAP2C play role in vascular remodeling [52], or improving cell damage by mediating miR-23a-5p/SFRP5/Wnt5a to inhibit autophagy [53], respectively. Therefore, we identified common TFs shared by the M2-like1 and M2-like1 subpopulations in DCM, and the candidate TFs with higher expression in the M2-like2 population than in the M2-like1 subpopulation.

In the Connectivity Map, we submitted the upregulated or downregulated gene sets of the M2-like2 cell subpopulation to screen small molecule compounds relevant to the M2-like2 cell subpopulation. Using this method, we found five potential small molecule drugs with therapeutic effects on the M2-like2 cell subpopulation, including quizartinib, alectinib, KIN-001-220, sertraline, doconexent, ruboxistaurin, rigosertib, duloxetine, anguidine, and BRD-K68552125 (Fig. 5H, Additional file 7: Table S19).

Metabolic specificity of non-cardiomyocytes in DCM

The immune metabolism and related biological phenotypes in DCM are still unclear. To understand non-cardiomyocytes metabolism in DCM, we calculated the scores of 77 active metabolic pathways using scMetabolism

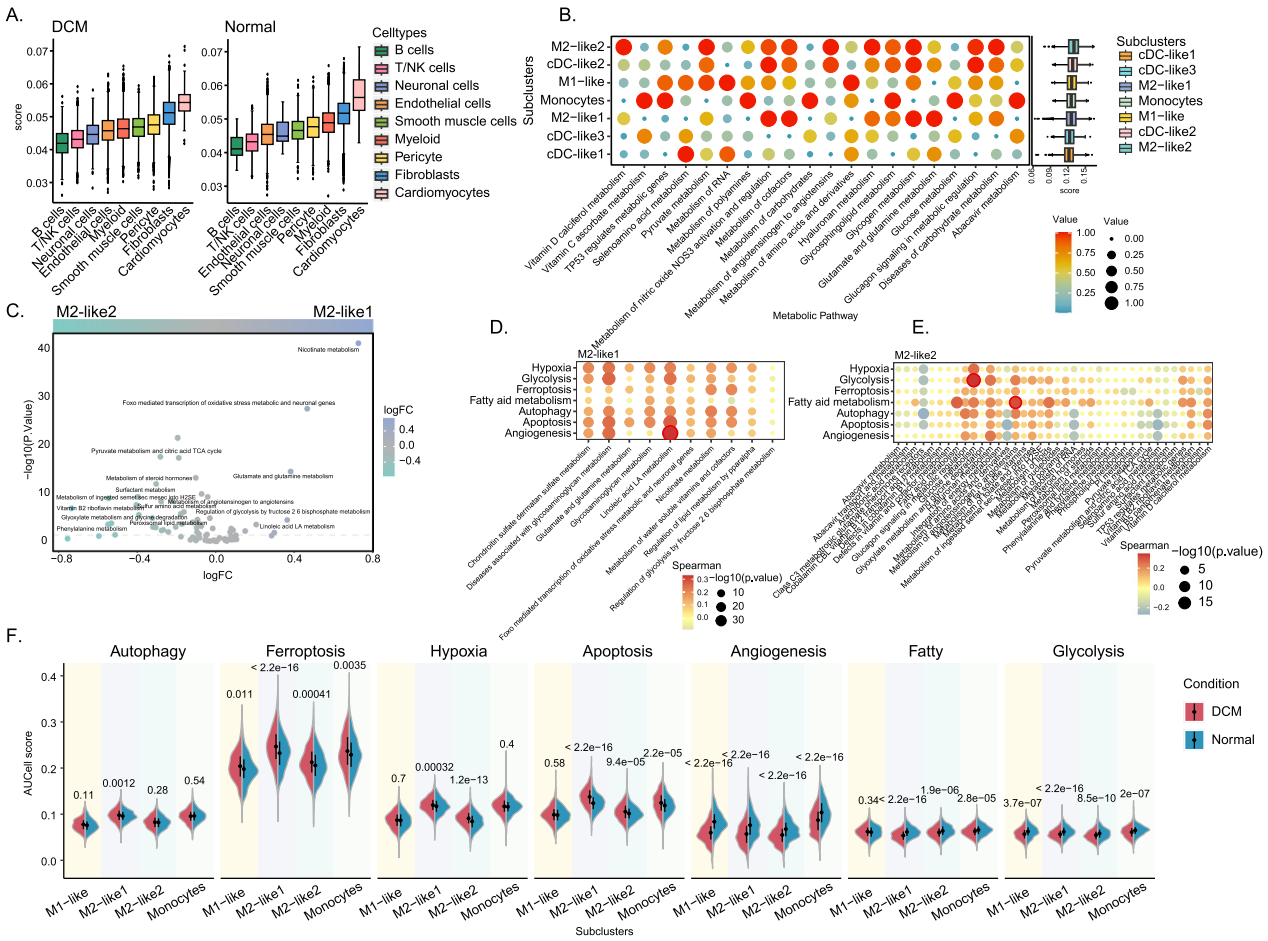

Fig. 6 Metabolic specificity of cell types. **A** DCM (left) and Normal(right) metabolic activity of 9 cell types. **B** Left: Top 20 metabolic pathway activities in myeloid cells; Right: All myeloid cells metabolic pathway activities. **C** Differential metabolic pathways between M2-like1 and M2-like2. **D** Correlations between phenotype scores and metabolic activity scores in M2-like1 macrophages. Red circles indicate P < 0.05, Spearman's rho > 0.3. **E** Correlations between phenotype scores and metabolic activity scores in M2-like2 macrophages. Red circles indicate P < 0.05, Spearman's rho > 0.3. **F** Phenotype scores of monocytes and macrophages

(Fig. 6A). Among all of cell types, fibroblasts and myeloid cells consistently showed high metabolic activity scores in both DCM and normal samples.

Then, we further investigated metabolic heterogeneity among different cell subpopulations in the myeloid lineage. The top 20 metabolic scores were selected from all the subpopulations for ranking the cell subpopulations based on the average metabolic score of all the pathways (Fig. 6B). We found that the M2-like2 cell subpopulation exhibited the highest metabolic activity among all myeloid cell subpopulations, while the M2-like1 macrophage subpopulation shown a low activity, which may attribute to specific functional differences among different macrophage subpopulations in DCM.

Moreover, further analysis revealed 10 upregulated metabolic pathways in the M2-like1 subpopulation and 38 upregulated metabolic pathways in the M2-like2 subpopulation ($P < 0.05$). Among them, glutamate and glutamine metabolism and sialic acid metabolism were highly expressed in M2-like1 (Fig. 6C, Additional file 7: Table S20). It has been reported that glutamine plays a crucial role in cardiovascular physiology and pathology, serving as a substrate for the synthesis of DNA, ATP, proteins, and lipids and driving key processes in vascular cells, including proliferation, migration, apoptosis, senescence, and extracellular matrix deposition, while sialic acid is an essential component of glycoproteins and glycolipids [54], exerting roles in cell communication, infection, and metastasis. On the other hand, pyruvate metabolism was highly expressed in M2-like2 macrophages, in which pyruvate is a natural fat-derived carbohydrate and intermediate metabolite produced in the cytosol through glycolysis or lactate oxidation. Pyruvate can produce energy and exert antioxidant and anti-inflammatory effects, collectively enhancing cardiac mechanical performance and protecting the myocardium from ischemic injury [55].

In the immune response, macrophages can differentiate into pro-inflammatory M1 and anti-inflammatory M2 types according to signals from the surrounding environment. M1 macrophages enhance glycolysis and decrease oxidative phosphorylation, while M2 macrophages rely on mitochondrial respiration and fatty acid oxidation. These metabolic differences reflect their distinct functions in the immune response. To demonstrate the relationship between metabolic reprogramming and macrophage phenotype changes, we next examined the association between the upregulated metabolic pathways in M2-like1 (10 pathways) and M2-like2 (38 pathways) and metabolic reprogramming. The specific metabolic processes of the M2-like1 subpopulation were associated with angiogenesis, while those of the M2-like2 subpopulation were related to glycolysis and fatty acid metabolism (Fig. 6D, E). We explored the extent of metabolic reprogramming in different subpopulations and found higher DCM scores in the M2-like1 and M2-like2 subpopulations subjected to ferroptosis, hypoxia, and apoptosis than in normal samples (Fig. 6F). Fatty acid metabolism was greater in M2-like2 than in M2-like1. In contrast, compared with M2-like2 macrophages, M2-like1 macrophages exhibit more autophagy, ferroptosis, hypoxia, apoptosis and glycolysis (Additional file 5: Fig. S5A-B). Hence, gaining a deeper understanding of the metabolic phenotypes of macrophages may help elucidate the mechanisms underlying of DCM and provide insights for future therapies.

Cell–cell communications

To evaluate the differences in molecular interactions between cells from different injured spatial locations, we constructed a cell–cell communication network based on known ligand–receptor pairs and their accessory factors using CellChat (Fig. 7A, B). We found that DCM samples showed more intercellular interactions than normal samples (Fig. 7C), possibly due to increased interactions of CMs and fibroblasts with other cell types and increased interactions between myeloid cells themselves in DCM (Additional file 6: Fig. S6A).

We observed a high level of communication not only between fibroblasts and other cells but also among myeloid cells. Next, by comparing cell communication between DCM and normal samples, we identified 24 enriched signaling pathways in DCM and normal samples (Fig. 7D). Among these pathways, the GAS signaling pathway was mainly enriched in DCM (Fig. 7D). GAS6 has been shown to play an important role in the heart by participating in immune regulation and inflammation activation through binding to AXL, regulating macrophage activation, promoting phagocytosis of apoptotic cells, aiding in platelet aggregation, and maintaining the stability of intravascular clots. The Gas6/Axl-AMPK signaling pathway protects against hydrogen peroxide-induced oxidative stress while also improving oxidative stress, cell apoptosis, and mitochondrial function [56]. Furthermore, a communication through GAS signals interaction between M2 macrophages and cDC-like1 cell subpopulations in DCM was also identified (Fig. 7E). Among known ligand–receptor pairs, M2 macrophages communicate with cDC-like1 through GAS6-AXL, while M2 macrophages communicate with M2-like1 through GAS6-MERTK in DCM. (Fig. 7F–H). We also conducted a detailed analysis for the changes in signaling receptor levels for all important pathways. The APP signaling pathway was significantly activated in DCM, which was mainly transmitted from the cDC-like3 cell subset

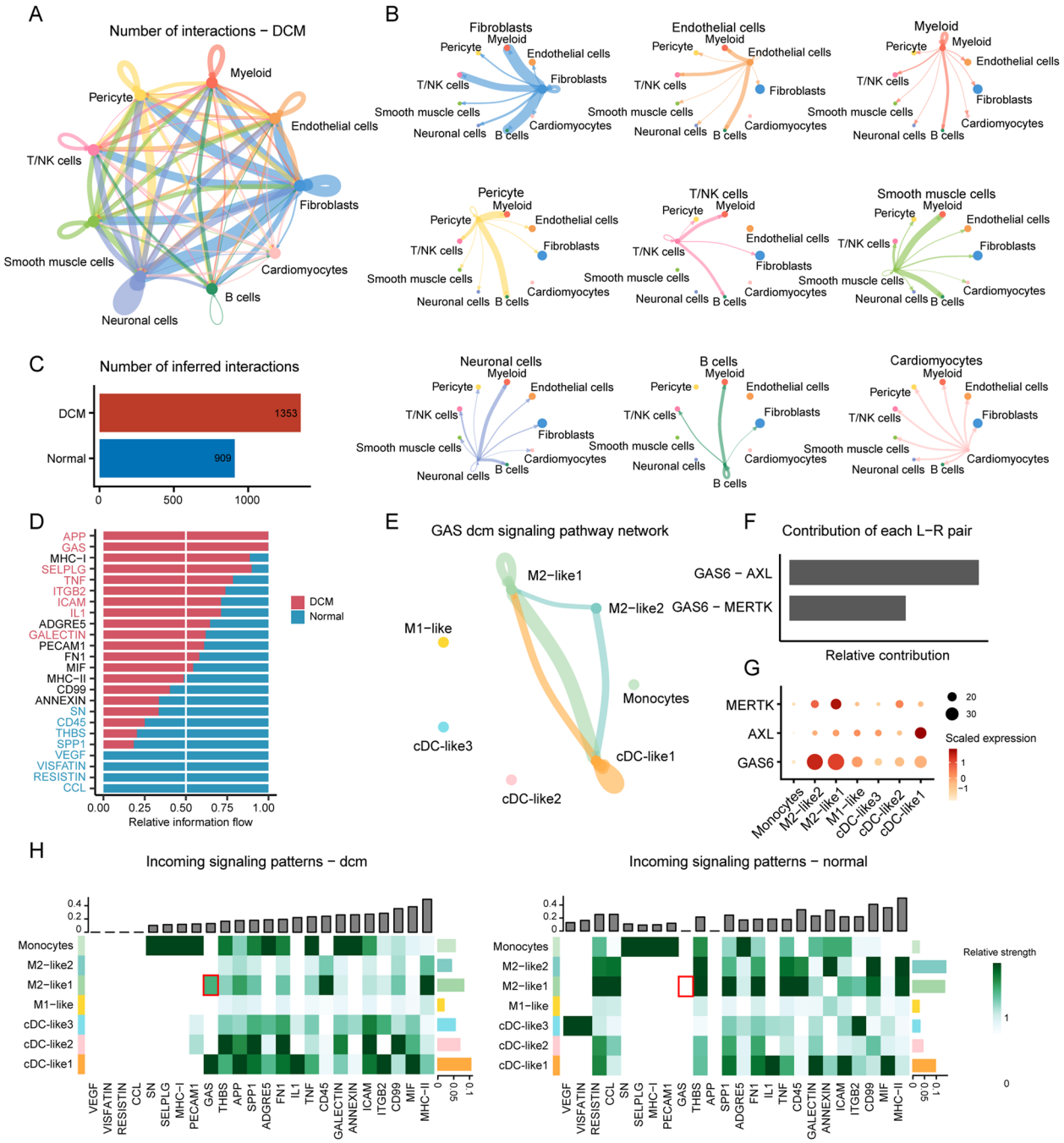

Fig. 7 Cell communication in cell types. **A** Circular plot showing the number of interactions between cell types in DCM patients. The thickness of the lines is proportional to the number of ligand–receptor interactions, and the loops represent autocrine loops. **B** Detailed view of ligand–receptor interactions in cell types involved in DCM. **C** Inferred number of ligand–receptor interactions between DCM and normal samples. **D** Total information flow and ranking of important signaling pathways in the network differences between DCM and normal samples. **E** Inferred GAS signaling network. Edge width represents the communication probability. **F** Relative contribution of each ligand–receptor pair to the overall communication network of the GAS signaling pathway. **G** Expression levels of ligands and receptors contributing to the GAS signaling pathway in myeloid cells. **H** Comparison of cell-incoming signaling patterns between DCM and normal samples. The colors are proportional to the contribution scores calculated from pattern recognition analysis. Higher scores indicate richer signaling pathways in the corresponding cell population

to other cells (Additional file 6: Fig. S6B). On the other hand, CCL, RESISTIN, VISFATIN, and VEGF signals were only present in normal samples (Additional file 6: Fig. S6C-F). The CCL signaling pathway largely targets M2 macrophages from cDC-like1, and other signaling mediated by RESISTIN, VISFATIN or VEGF is for other myeloid cells from M2-like2, the cDC-like3 cell subset from other myeloid cells, and the cDC-like3 cell subset from M2-like1 cells only in macrophages,respectively.

Finally, to validate the role of the GAS6-MERTK interaction in DCM, we examined the expression levels of GAS6 and MERTK in the GSE14191 and GSE116250 datasets. GAS6 expression was significantly greater in DCM samples than in normal samples, consistent with our results (Additional file 6: Fig. S6G). Overall, these findings confirm the high expression of GAS6 in M2-like1 macrophages in DCM and the interaction of GAS6 with cDC-like1 and M2-like1 through AXL and MERTK, thus activation of the GAS6-MERTK axis plays a crucial role in DCM.

Discussion

In this study, we provided a detailed evaluation on the alternations in non-cardiomyocytes in DCM. Based on bulk data from 322 samples, we predicted cell composition and observed significant differences between DCM and normal samples in fibroblasts, T cells, NK cells, and myeloid cells. Subsequently, we integrated two human single-cell RNA-seq datasets and conducted detailed analyses for these three cell types at the single-cell level, demonstrating the complex heterogeneity in DCM microenvironment.

By analysis of the single-cell data from normal and DCM samples, we identified 9 cell types, in which fibroblasts, T cells, NK cells, and myeloid cells were further divided into different subpopulations based on functionality and cell states. Through evaluating the functional characteristics and potential regulatory relationships in myeloid cell subpopulations, M2-like1 and M2-like2 were detailly broke down for the first time. Additionally, we constructed landscapes of cell metabolism and communication using the data, providing insights for DCM personalized diagnosis and treatment.

Cardiac fibroblasts as essential cellular components of heart play a crucial role in DCM development via depositing collagen and other extracellular matrix components [57]. The fibroblasts are also responsible for cardiac remodeling and fibrosis following cardiac injury. In this study, we utilized scRNA-seq technology to integrate data on cardiac fibroblasts, providing a preliminary understanding for the alternations in the cell type in DCM. The results are consistent with that resident cardiac fibroblasts as the main source of activated fibroblasts are involved in cardiac tissue fibrosis and remodeling [40], providing a clue again for non-cardiomyocytes role in heart diseases.

Moreover, we identified a total of 26,435 cardiac fibroblasts from both DCM and normal samples, in which 5,763 F1 cells, 4,329 F2 cells, and 2,031 F5 cells were in a resting state. Some F2 cells were in an activated state, while 3,924 F3 cells were proliferative fibroblasts. Additionally, 986 F6 cells was in a fibrotic state. These different subpopulations of cardiac fibroblasts exhibit distinct functions. For example, the F1 cell subpopulation mainly enriched in cell cycle-related processes highly expressed the genes for embryonic development and the control of myocardial fibrosis. The F2 cell subpopulation contained both resting and activated fibroblasts. Activated F2 cells branched from the resting F2 subpopulation in the pseudotime trajectory of fibroblast. The F3 subpopulation spans the beginning and end of the pseudotime trajectory of cellular states, with highly expressed genes involved in cell proliferation, migration, adhesion, and attachment. Notably, the significant overexpression of the *POSTN* gene in the F3 subpopulation increased the risk of cardiac fibrosis, which is consistent with previous reports [58]. The F5 subpopulation is involved in complement activation, the alternative pathway, complement and coagulation cascades, complement-dependent cytotoxicity, and stimulating inflammation. The F6 subpopulation showed high expression of fibrosis markers such as *COL1A1*, which is typical of fibrotic fibroblasts. Overall, the F6 and F3 subpopulations were more prevalent in DCM, while the F5 subpopulation was less common, thus providing more evidence for previous findings.

Generally, cardiac injury induces a local migration of cardiac cells, and extracardiac immune cells migrate intracellularly. By comprehensively analyzing T cells and NK cells, we here identified 2 CD4+T cell subpopulations (CD4-C1-CDKN1A and CD4-C2-RGS1), 7 CD8+T cell subpopulations (CD8-C1-HSPA1B, CD8-C2-FGFBP2, CD8-C3-GZMK, CD8-C4-FGFBP2, CD8-C5-FABP4, CD8-C6-XCL1, and CD8-C7-STMN1), 2 NK cell subpopulations (NK1 and NK2), 1 naive T cell subpopulation (Naive T), and other T cell-like subpopulations (MONO, FIB1, FIB2, DC). CD4-C1-CDKN1A is significantly related to DCM, participating in the regulation of activated T cells, the positive regulation of cytokines, and adhesion molecule binding, as well as the cell phagocytosis pathway that is a typical feature of DCM [59]. According to our analysis results of the pseudotime trajectory, CD4-C1-CDKN1A cells exhibited greater differentiation potential than CD4-C2-RGS1 cells. Similarly, CD8-C1-FGFBP2 was significantly expressed in DCM and enriched in focal adhesion, an important step in cell migration [60]. Compared to other

CD8 + T cell subpopulations, CD8-C1-FGFBP2 had lower differentiation potential and was located at the end of the pseudotime differentiation model. It is worth noting that a significant upregulation of TXNIP gene in both CD4 + and CD8 + cells is associated with inflammation, which may exert a role to protect the heart from damage [44].

On the other hand, we also provided a comprehensive landscape of myeloid cells at the single-cell level. Totally, 11 cell subpopulations, including 3 dendritic cell subpopulations, 3 macrophage subpopulations, 1 classical monocyte subpopulation, and other cell-like subpopulations were identified. Among them, two M2-like macrophage subpopulations were previously unreported. M2-like1 significantly appeared in reactions to topological errors and unfolded proteins, as well as in functions related to muscle tissue and organ development, which with upregulated genes, such as *SNHG12* [61] and *HSPA6* [62], promoted immune escape, or M2 polarization by *WDR74* [63] and *DDIT3* [64]. The M2-like1 subpopulation was also correlated with the transcription factor NFIA, a risk factor for heart failure [51]. The functions of M2-like2 was related to antigen processing and presentation through MHC class II, with highly expressed genes, including *MARCKS*, *ALDHA1*, and *TMEM173*, to take part in inflammation inhibition [65], cell migration promotion [49], and fibrosis promotion [50]. Transcription factors related to M2-like2, such as HOXB5, TFAP2C, ETV5, and NFIA, promote vascular remodeling and inhibit autophagy, which really shown higher expression in DCM samples than in normal samples. All the results point out various functions of M2-like1 subpopulation in DCM, while the M2-like2 subpopulation only has a single function as a signature subpopulation of DCM.

Non-cardiomyocytes, including fibroblasts, pericytes, and myeloid cells also increased metabolic activity. Among myeloid cells, the M2-like2 subpopulation shown the highest metabolic activity in pathways such as vitamin B2 riboflavin metabolism, phenylalanine metabolism, and sulfur amino acid metabolism etc. Previous evidences have strongly linked ATP metabolism defects to heart failure [66, 67] due to reduced expression of creatine kinase and complex I in animal models and the patient hearts [68]. Heart failure has been suggested to be prevented by targeting alternative mitochondrial creatine kinase or mitochondrial-targeted inhibition of CaMKII [68]. Here, we revealed that the M2-like2 subpopulation exhibited specific acetone metabolism, producing natural fat carbohydrates through glycolysis to enhance cardiac mechanical performance for protecting the heart from ischemic injury. Multi-omics analyses have also identified pyruvate as a biomarker for heart failure [69]. Further analysis found that the increase of glycolytic activity of M2-like2 may be related to glucose metabolism, while the increase of fatty acid metabolism may be involved in the metabolism of angiotensinogen to angiotensins. In glycolysis, glucose is broken down into pyruvate in the cytoplasm under anaerobic conditions, which produces ATP to provide energy for the organism. Fatty acid, glucose, or ketone metabolism might provide clinical benefits to patients with heart failure [70]. The adult heart utilizes fatty acids as a principal fuel source, but it can also get energy from glucose and ketone, and to some degree from lactate, pyruvate, and amino acids. Nevertheless, myocardial cells of the failing heart can withstand incredible metabolic remodeling that includes a change in substrate usage and decreased ATP production, which explain cardiac remodeling and abnormal systolic function. The principal therapeutic metabolic strategies comprise blocking fatty acid oxidation, decreasing circulating fatty acid concentrations, augmenting glucose oxidation, and enhancing ketone oxidation [71]. Therefore, M2-like2 is really associated with the final step of glycolysis.

Cell–cell communication network analysis also detected the close correlations between different cell ligands and receptors, indicating that different tissue cells may form different communication patterns. Compared with normal samples, DCM samples exhibit more intercellular interactions, in which fibroblasts mainly mediate signals to T cells, myeloid cells, and B cells. In DCM, M2-like2 can trigger GAS signal to dendritic cells and the M2-like1 subpopulation of cells. GAS6 signaling participates in immune regulation and inflammation activation through AXL binding, while its interaction with MERTK regulates macrophage activation, indicating its potential as a biomarker for DCM.

However, this study has certain limitations. Both single-cell data and bulk data were obtained from public datasets with limited number of patients. We only revealed heterogeneity related to DCM, without considering clinical phenotypes or disease progression. Focusing only on one state comparison may ignore the dynamic nature of disease progression. Disease states are relying on a snapshot from a single state can miss transitional phases and complex regulatory mechanisms. In metabolic analysis, we conducted indirect analysis without detailed investigation. Finally, this study did not include in vitro or in vivo experiments, and clinical samples were not applied for result validation. Hence, An analysis with more sophisticated single-cell multi-omics workflow combining additional experiments need to perform for validate our findings.

Conclusions

In this research, we constructed a comprehensive single-cell transcriptional atlas of DCM, revealing significant heterogeneity among non-cardiomyocytes populations in DCM pathogenesis. By applying multiple computational algorithms, we uncovered critical roles for novel M2 macrophage subsets in disease. These findings highlight the potential of specific cell populations as biomarkers and therapeutic targets for DCM, provide insights into the occurrence of DCM and offer reference for personalized treatment of the disease.

Abbreviations

DCM	Dilated cardiomyopathy
pctMT	Percentage of mitochondrial genes
scRNA-seq	Single-cell RNA sequencing
HVGs	Highly variable genes
t-SNE	T-distributed stochastic neighbor embedding
DEGs	Differentially expressed genes
EPIC	Estimating the proportion of immune and cancer cells
SVR	Support vector regression
MCPcounter	Microenvironment cell populations counter
ssGSEA	Single-sample gene set enrichment analysis
GSE	Gene set enrichment score
OR	Odds ratio
SCENIC	Single-cell regulatory network inference and clustering
RSS	Regulatory activity scores
GSEA	Gene set enrichment analysis
MsigDB	Molecular signatures database
HADb	Human autophagy database
FDR	False discovery rate

Supplementary Information

The online version contains supplementary material available at https://doi.org/10.1186/s12967-024-05983-1.

Additional file 1: Figure S1. Single-cell data reveal the landscape in DCM and normal samples. A. PCA plots of scRNA-seq data colored by sex (top) and age (bottom). Each data point represents an individual. "Young": under 40 years old, "Middle": between 40 and 60 years, "Old": over 60 years old. B.t-SNE plot showing clustering of single-cell samples into 23 clusters. C. t-SNE plot displaying the cellular distribution of 70,958 DCM and normal samples. D. Cell type-specific gene expression values for each cell type. E. Heatmap showing the top 20 DEGs in each cell type. F. Preference of tissue morbidity rates estimated by Ro/e scores for each cell type. G. Boxplot showing cell purity for each cell type by ROGUE.

Additional file 2: Figure S2. Cell infiltration analysis. CIBERSORT (A), EPIC (B), MCP (C), xCell (D) counts distinct cell abundances in the GSE141910 cohort. E.xCell counts distinct cell abundances in the van Heesch et al dataset. The bold line represents the median. The bottom and top of the boxes are the 25th and 75th percentiles (interquartile ranges), respectively.

Additional file 3: Figure S3. A single-cell atlas of fibroblasts. A. Heatmap showing the top 10 differentially expressed genes in fibroblast subtypes. B. Left, heatmap depicting the expression patterns of differentially expressed genes in fibroblasts based on the pseudotime trajectory; from blue to red represents low to high expression patterns. Right, GO analysis for Cluster 1. C. Functional enrichment levels of fibroblast subtypes. D. Pathway enrichment levels of fibroblast subtypes.

Additional file 4: Figure S4. A single-cell atlas of T cells A. Violin plots showing the proportional expression levels of typical markers used for identifying each cell subpopulations. B. Computational ordering according to the gradual transition of transcriptomes enabled clustering CD4+ T cells into pseudotemporal states. C-D. Left, heatmap depicting DEGs in CD4+ T cells at branch point one (C) and branch point two (D) based on the pseudotime trajectory; genes from blue to red represent low to high expression patterns; right, GO analysis. E. Dynamic expression of differentially expressed genes in CD4+ T cells within pseudotime. F. Computational ordering according to the gradual transition of transcriptomes enabled clustering CD8+ T cells into pseudotemporal states. G. Left, heatmap depicting DEGs in CD8+ T cells at branch point two based on the pseudotime trajectory; genes from blue to red represent low to high expression patterns; right, GO analysis for cluster 5. H. Dynamic expression of differentially expressed genes in CD8+ T cells within pseudotime. I. Volcano plot showing DEGs between the NK1 and NK2 subtypes and the other subtypes. Red indicates upregulation relative to other subtypes, and blue indicates downregulation. J. Feature plots showing the expression of canonical cell marker genes used to define each cluster. K. Pathway and functional enrichment of the NK1 and NK2 subtypes.

Additional file 5: Figure S5. Metabolic activity of DCM and normal samples. A-B. Aucell method to calculate the metabolic activity of DCM (A) and normal samples (B).

Additional file 6: Figure S6. Communication among myeloid cell subtypes. A. Inferred number of ligand–receptor interactions among different cell types. B-F. The inferred APP (B), CCL (C), RESISTIN (D), VISFATIN (E) and VEGF (F) signaling networks. Edge width represents the communication probability. G. Expression of the GAS6 and MERTK genes in the GSE141910 and GSE116250 datasets. Red represents DCM samples, and blue represents normal samples.

Additional file 7: Table S1-S20. Table S1. The clinical information of samples included in the present study. Table S2. DEGs between dcm and normal patients in all celltypes. Table S3-S4. DEGs in all celltypes (Table S3), Fibroblast (Table S4). Table S5-S6. GO Enrichment analysis of branch 1 (Table S5) and branch 2 (Table S6) in Fibroblast. Table S7. DEGs in development of fibroblasts cell state. Table S8. DEGs in T Cells. Table S9. GO and KEGG enrichment analysis of DEGs in T Cells. Table S10. GO enrichment analysis of branch 1 (Table S10) and branch 2 (Table S11) in CD4+T Cells. Table S12. GO enrichment analysis of branch 1 in CD8+T Cells. Table S13. DEGs in NK cells. Table S14. GO and KEGG enrichment analysis of DEGs in NK Cells. Table S15. DEGs in myeloid cells. Table S16. GO and KEGG enrichment analysis of DEGs in myeloid cells. Table S17. DEGs between DCM and normal samples in myeloid cells. Table S18. GO enrichment analysis of branch 1 in myeloid cells. Table S19. Similarity scores of drug-disease pairs. Table S20. Differential metabolism of M2-like1 and M2-like2 in DCM.

Author contributions

SHe and LL contributed to the conception and design; LP and LL contributed financial support; SHe and CL contributed to data analysis and interpretation; FL, ML and JZ helped perform the analysis with constructive discussions; SHe and SHu contributed to analysis and manuscript preparation; LP and LL approved the final version of the manuscript. All authors read and approved the final manuscript.

Funding

This research was supported by the National Natural Science Foundation of China (824704088, 82070270, 32071109), the National Key Research and Development Program (2022YFE0100400), the Shanghai Committee of Science and Technology (22ZR1463800). Li Li is a Fellow at the Collaborative Innovation Center For Cardiovascular Disease Translational Medicine, Nanjing Medical University.

Availability of data and materials

The datasets generated analyzed during the current study are available in the GEO repository, including GSE183852, GSE145154, GSE1145 and GSE116250.

Declarations

Ethics approval and consent to participate

Not applicable.

Consent for publication

Not applicable.

Competing interests
The authors declare that they have no competing interests in this section.

Author details
[1]State Key Laboratory of Cardiovascular Diseases and Medical Innovation Center, School of Medicine, Shanghai East Hospital, Tongji University, Shanghai 200120, China. [2]Shanghai Arrhythmias Research Center, Shanghai East Hospital, Tongji University School of Medicine, Shanghai 200120, China. [3]Stem Cell Research Center, Medical School, Tongji University, Shanghai 200120, China. [4]Department of Cell and Genetics, Tongji University School of Medicine, Shanghai 200120, China.

Received: 9 August 2024 Accepted: 13 December 2024
Published online: 06 January 2025

References

1. Richardson P, McKenna W, Bristow M, Maisch B, Mautner B, O'Connell J, et al. Report of the 1995 World Health Organization/International Society and Federation of Cardiology Task Force on the definition and classification of cardiomyopathies. Circulation. 1996;93(5):841–2.
2. Marchant DJ, Boyd JH, Lin DC, Granville DJ, Garmaroudi FS, McManus BM. Inflammation in myocardial diseases. Circ Res. 2012;110(1):126–44.
3. Escher F, Kühl U, Lassner D, Stroux A, Westermann D, Skurk C, et al. Presence of perforin in endomyocardial biopsies of patients with inflammatory cardiomyopathy predicts poor outcome. Eur J Heart Fail. 2014;16(10):1066–72.
4. Banerjee I, Fuseler JW, Price RL, Borg TK, Baudino TA. Determination of cell types and numbers during cardiac development in the neonatal and adult rat and mouse. Am J Physiol Heart Circ Physiol. 2007;293(3):H1883-1891.
5. Bergmann O, Zdunek S, Felker A, Salehpour M, Alkass K, Bernard S, et al. Dynamics of cell generation and turnover in the human heart. Cell. 2015;161(7):1566–75.
6. Pinto AR, Ilinykh A, Ivey MJ, Kuwabara JT, D'Antoni ML, Debuque R, et al. Revisiting cardiac cellular composition. Circ Res. 2016;118(3):400–9.
7. Nag AC. Study of non-muscle cells of the adult mammalian heart: a fine structural analysis and distribution. Cytobios. 1980;28(109):41–61.
8. Perbellini F, Watson SA, Scigliano M, Alayoubi S, Tkach S, Bardi I, et al. Investigation of cardiac fibroblasts using myocardial slices. Cardiovasc Res. 2018;114(1):77–89.
9. Ni SH, Xu JD, Sun SN, Li Y, Zhou Z, Li H, et al. Single-cell transcriptomic analyses of cardiac immune cells reveal that Rel-driven CD72-positive macrophages induce cardiomyocyte injury. Cardiovasc Res. 2022;118(5):1303–20.
10. Ruiz-Villalba A, Romero JP, Hernández SC, Vilas-Zornoza A, Fortelny N, Castro-Labrador L, et al. Single-cell RNA sequencing analysis reveals a crucial role for CTHRC1 (collagen triple helix repeat containing 1) cardiac fibroblasts after myocardial infarction. Circulation. 2020;142(19):1831–47.
11. Cartledge JE, Kane C, Dias P, Tesfom M, Clarke L, McKee B, et al. Functional crosstalk between cardiac fibroblasts and adult cardiomyocytes by soluble mediators. Cardiovasc Res. 2015;105(3):260–70.
12. Bang C, Batkai S, Dangwal S, Gupta SK, Foinquinos A, Holzmann A, et al. Cardiac fibroblast-derived microRNA passenger strand-enriched exosomes mediate cardiomyocyte hypertrophy. J Clin Invest. 2014;124(5):2136–46.
13. Tang F, Barbacioru C, Wang Y, Nordman E, Lee C, Xu N, et al. mRNA-seq whole-transcriptome analysis of a single cell. Nat Methods. 2009;6(5):377–82.
14. Skelly DA, Squiers GT, McLellan MA, Bolisetty MT, Robson P, Rosenthal NA, et al. Single-cell transcriptional profiling reveals cellular diversity and intercommunication in the mouse heart. Cell Rep. 2018;22(3):600–10.
15. McLellan MA, Skelly DA, Dona MSI, Squiers GT, Farrugia GE, Gaynor TL, et al. High-resolution transcriptomic profiling of the heart during chronic stress reveals cellular drivers of cardiac fibrosis and hypertrophy. Circulation. 2020;142(15):1448–63.
16. Samad T, Wu SM. Single cell RNA sequencing approaches to cardiac development and congenital heart disease. Semin Cell Dev Biol. 2021;118:129–35.
17. Gladka MM, Molenaar B, de Ruiter H, van der Elst S, Tsui H, Versteeg D, et al. Single-cell sequencing of the healthy and diseased heart reveals cytoskeleton-associated protein 4 as a new modulator of fibroblasts activation. Circulation. 2018;138(2):166–80.
18. Aran D, Hu Z, Butte AJ. xCell: digitally portraying the tissue cellular heterogeneity landscape. Genome Biol. 2017;18(1):220.
19. Newman AM, Liu CL, Green MR, Gentles AJ, Feng W, Xu Y, et al. Robust enumeration of cell subsets from tissue expression profiles. Nat Methods. 2015;12(5):453–7.
20. Racle J, Gfeller D. EPIC: a tool to estimate the proportions of different cell types from bulk gene expression data. Methods Mol Biol. 2020;2120:233–48.
21. Becht E, Giraldo NA, Lacroix L, Buttard B, Elarouci N, Petitprez F, et al. Estimating the population abundance of tissue-infiltrating immune and stromal cell populations using gene expression. Genome Biol. 2016;17(1):218.
22. Zhang Q, He Y, Luo N, Patel SJ, Han Y, Gao R, et al. Landscape and dynamics of single immune cells in hepatocellular carcinoma. Cell. 2019;179(4):829-845.e820.
23. van Heesch S, Witte F, Schneider-Lunitz V, Schulz JF, Adami E, Faber AB, et al. The translational landscape of the human heart. Cell. 2019;178(1):242-260.e229.
24. Zhao J, Gao JL, Zhu JX, Zhu HB, Peng X, Jiang M, et al. The different response of cardiomyocytes and cardiac fibroblasts to mitochondria inhibition and the underlying role of STAT3. Basic Res Cardiol. 2019;114(2):12.
25. Huang CC, Kuo HM, Wu PC, Cheng SH, Chang TT, Chang YC, et al. Soluble delta-like 1 homolog (DLK1) stimulates angiogenesis through Notch1/Akt/eNOS signaling in endothelial cells. Angiogenesis. 2018;21(2):299–312.
26. Rodriguez P, Sassi Y, Troncone L, Benard L, Ishikawa K, Gordon RE, et al. Deletion of delta-like 1 homologue accelerates fibroblast-myofibroblast differentiation and induces myocardial fibrosis. Eur Heart J. 2019;40(12):967–78.
27. Schellings MW, Pinto YM, Heymans S. Matricellular proteins in the heart: possible role during stress and remodeling. Cardiovasc Res. 2004;64(1):24–31.
28. Yuting Y, Lifeng F, Qiwei H. Secreted modular calcium-binding protein 2 promotes high fat diet (HFD)-induced hepatic steatosis through enhancing lipid deposition, fibrosis and inflammation via targeting TGF-β1. Biochem Biophys Res Commun. 2019;509(1):48–55.
29. Dixon IMC, Landry NM, Rattan SG. Periostin reexpression in heart disease contributes to cardiac interstitial remodeling by supporting the cardiac myofibroblast phenotype. Adv Exp Med Biol. 2019;1132:35–41.
30. Vanhoutte D, Schips TG, Vo A, Grimes KM, Baldwin TA, Brody MJ, et al. Thbs1 induces lethal cardiac atrophy through PERK-ATF4 regulated autophagy. Nat Commun. 2021;12(1):3928.
31. Rizzi F, Caccamo AE, Belloni L, Bettuzzi S. Clusterin is a short half-life, polyubiquitinated protein, which controls the fate of prostate cancer cells. J Cell Physiol. 2009;219(2):314–23.
32. Itoh N, Ornitz DM. Fibroblast growth factors: from molecular evolution to roles in development, metabolism and disease. J Biochem. 2011;149(2):121–30.
33. Pagano F, Angelini F, Castaldo C, Picchio V, Messina E, Sciarretta S, et al. Normal versus pathological cardiac fibroblast-derived extracellular matrix differentially modulates cardiosphere-derived cell paracrine properties and commitment. Stem Cells Int. 2017;2017:7396462.
34. Duca L, Blaise S, Romier B, Laffargue M, Gayral S, El Btaouri H, et al. Matrix ageing and vascular impacts: focus on elastin fragmentation. Cardiovasc Res. 2016;110(3):298–308.
35. Guthold M, Liu W, Sparks EA, Jawerth LM, Peng L, Falvo M, et al. A comparison of the mechanical and structural properties of fibrin fibers with other protein fibers. Cell Biochem Biophys. 2007;49(3):165–81.
36. Barrett-Connor E. Gender differences and disparities in all-cause and coronary heart disease mortality: epidemiological aspects. Best Pract Res Clin Endocrinol Metab. 2013;27(4):481–500.
37. Ang LS, Cruz RP, Hendel A, Granville DJ. Apolipoprotein E, an important player in longevity and age-related diseases. Exp Gerontol. 2008;43(7):615–22.
38. Cao J, Zou H, Zhu BP, Wang H, Li J, Ding Y, et al. Sex hormones and androgen receptor: risk factors of coronary heart disease in elderly men. Chin Med Sci J. 2010;25(1):44–9.

39. Enzan N, Matsushima S, Ikeda S, Okabe K, Ishikita A, Yamamoto T, et al. ZBP1 protects against mtDNA-induced myocardial inflammation in failing hearts. Circ Res. 2023;132(9):1110–26.
40. Moore-Morris T, Guimarães-Camboa N, Banerjee I, Zambon AC, Kisseleva T, Velayoudon A, et al. Resident fibroblast lineages mediate pressure overload-induced cardiac fibrosis. J Clin Invest. 2014;124(7):2921–34.
41. Shuvalova YA, Khasanova ZB, Kaminnaya VI, Samoilova EV, Korotaeva AA, Rubanovich AV, et al. The association of PLA2G2A single nucleotide polymorphisms with type IIa secretory phospholipase A2 level but not its activity in patients with stable coronary heart disease. Gene. 2015;564(1):29–34.
42. Jordan E, Peterson L, Ai T, Asatryan B, Bronicki L, Brown E, et al. Evidence-based assessment of genes in dilated cardiomyopathy. Circulation. 2021;144(1):7–19.
43. Lee J, Termglinchan V, Diecke S, Itzhaki I, Lam CK, Garg P, et al. Activation of PDGF pathway links LMNA mutation to dilated cardiomyopathy. Nature. 2019;572(7769):335–40.
44. Nakayama Y, Mukai N, Wang BF, Yang K, Patwari P, Kitsis RN, et al. Txnip C247S mutation protects the heart against acute myocardial infarction. J Mol Cell Cardiol. 2021;155:36–49.
45. Crinier A, Narni-Mancinelli E, Ugolini S, Vivier E. SnapShot: natural killer cells. Cell. 2020;180(6):1280-1280.e1281.
46. Böttcher JP, Bonavita E, Chakravarty P, Blees H, Cabeza-Cabrerizo M, Sammicheli S, et al. NK cells stimulate recruitment of cDC1 into the tumor microenvironment promoting cancer immune control. Cell. 2018;172(5):1022-1037.e1014.
47. Xia P, Ji X, Yan L, Lian S, Chen Z, Luo Y. Roles of S100A8, S100A9 and S100A12 in infection, inflammation and immunity. Immunology. 2024;171(3):365–76.
48. Kim GD, Das R, Rao X, Zhong J, Deiuliis JA, Ramirez-Bergeron DL, et al. CITED2 restrains proinflammatory macrophage activation and response. Mol Cell Biol. 2018;38(5): e00452.
49. Li J, Chen YH, Li LZ, Wang F, Song W, Alolga RN, et al. Omics and transgenic analyses reveal that salvianolic acid B exhibits its anti-inflammatory effects through inhibiting the mincle-syk-related pathway in macrophages. J Proteome Res. 2021;20(7):3734–48.
50. De Vito A, Orecchia P, Balza E, Reverberi D, Scaldaferri D, Taramelli R, et al. Overexpression of murine Rnaset2 in a colon syngeneic mouse carcinoma model leads to rebalance of intra-tumor M1/M2 macrophage ratio, activation of T cells, delayed tumor growth, and rejection. Cancers. 2020;12(3):717.
51. Heaton MP, Harhay GP, Bassett AS, Clark HJ, Carlson JM, Jobman EE, et al. Association of ARRDC3 and NFIA variants with bovine congestive heart failure in feedlot cattle. F1000Research. 2022;11:385.
52. Fessner A, Esser JS, Bluhm F, Grundmann S, Zhou Q, Patterson C, et al. The transcription factor HoxB5 stimulates vascular remodelling in a cytokine-dependent manner. Cardiovasc Res. 2014;101(2):247–55.
53. Zeng M, Wei X, He YL, Chen JX, Lin WT. TFAP2C inhibits cell autophagy to alleviate myocardial ischemia/reperfusion injury by regulating miR-23a-5p/SFRP5/Wnt5a axis. FASEB J. 2023;37(6): e22959.
54. Wen XY, Tarailo-Graovac M, Brand-Arzamendi K, Willems A, Rakic B, Huijben K, et al. Sialic acid catabolism by N-acetylneuraminate pyruvate lyase is essential for muscle function. JCI Insight. 2018;3(24): e122373.
55. Mallet RT, Olivencia-Yurvati AH, Bünger R. Pyruvate enhancement of cardiac performance: cellular mechanisms and clinical application. Exp Biol Med. 2018;243(2):198–210.
56. Liang Z, Yang Y, Wu X, Lu C, Zhao H, Chen K, et al. GAS6/Axl is associated with AMPK activation and attenuates H(2)O(2)-induced oxidative stress. Apoptosis. 2023;28(3–4):485–97.
57. Tallquist MD. Cardiac fibroblast diversity. Annu Rev Physiol. 2020;82:63–78.
58. Koenig AL, Shchukina I, Amrute J, Andhey PS, Zaitsev K, Lai L, et al. Single-cell transcriptomics reveals cell-type-specific diversification in human heart failure. Nat Cardiovasc Res. 2022;1(3):263–80.
59. Sweet ME, Cocciolo A, Slavov D, Jones KL, Sweet JR, Graw SL, et al. Transcriptome analysis of human heart failure reveals dysregulated cell adhesion in dilated cardiomyopathy and activated immune pathways in ischemic heart failure. BMC Genom. 2018;19(1):812.
60. Paluch EK, Aspalter IM, Sixt M. Focal adhesion-independent cell migration. Annu Rev Cell Dev Biol. 2016;32:469–90.
61. Qian M, Ling W, Ruan Z. Long non-coding RNA SNHG12 promotes immune escape of ovarian cancer cells through their crosstalk with M2 macrophages. Aging. 2020;12(17):17122–36.
62. Li P, Gao X, Huang D, Gu X. Identification and characterization of prognostic macrophage subpopulations for human esophageal carcinoma. Curr Med Chem. 2024. https://doi.org/10.2174/0109298673284207240108105724.
63. Geng K, Ma X, Jiang Z, Gu J, Huang W, Wang W, et al. WDR74 facilitates TGF-β/Smad pathway activation to promote M2 macrophage polarization and diabetic foot ulcer wound healing in mice. Cell Biol Toxicol. 2023;39(4):1577–91.
64. Geng H, Zhang H, Cheng L, Dong S. Sivelestat ameliorates sepsis-induced myocardial dysfunction by activating the PI3K/AKT/mTOR signaling pathway. Int Immunopharmacol. 2024;128:111466.
65. Tomita Y, Anzai F, Misaka T, Ogawara R, Ichimura S, Wada K, et al. Targeting N-myristoylation through NMT2 prevents cardiac hypertrophy and heart failure. JACC Basic Transl Sci. 2023;8(10):1263–82.
66. Beer M, Seyfarth T, Sandstede J, Landschütz W, Lipke C, Köstler H, et al. Absolute concentrations of high-energy phosphate metabolites in normal, hypertrophied, and failing human myocardium measured noninvasively with (31)P-SLOOP magnetic resonance spectroscopy. J Am Coll Cardiol. 2002;40(7):1267–74.
67. Kumar AA, Kelly DP, Chirinos JA. Mitochondrial dysfunction in heart failure with preserved ejection fraction. Circulation. 2019;139(11):1435–50.
68. Luczak ED, Wu Y, Granger JM, Joiner MA, Wilson NR, Gupta A, et al. Mitochondrial CaMKII causes adverse metabolic reprogramming and dilated cardiomyopathy. Nat Commun. 2020;11(1):4416.
69. Gladding PA, Cooper M, Young R, Loader S, Smith K, Zarate E, et al. Metabolomics and a breath sensor identify acetone as a biomarker for heart failure. Biomolecules. 2022;13(1):1–13.
70. Yurista SR, Chen S, Welsh A, Tang WHW, Nguyen CT. Targeting myocardial substrate metabolism in the failing heart: ready for prime time? Curr Heart Fail Rep. 2022;19(4):180–90.
71. Manolis AS, Manolis TA, Manolis AA. Ketone bodies and cardiovascular disease: an alternate fuel source to the rescue. Int J Mol Sci. 2023;24(4):3534.

Publisher's Note